U–Pb geochronology and trace-element composition of zircons from the Jinchang Au–Ni deposit, SW China, and their implications for tectonics

Lingang Xu[1] , Zhigang Kong[2], Jianfei Qu[1], Zhiyin Qiu[1] and Jianfeng Gao[3]

[1]State Key Laboratory of Geological Processes and Mineral Resources, China University of Geoscience, 100083 Beijing, China; [2]Faculty of Land Resource Engineering, Kunming University of Science and Technology, 650093 Kunming, China and [3]State Key Laboratory of Ore Deposit Geochemistry, Institute of Geochemistry, Chinese Academy of Sciences, Guiyang 550002, China

Abstract

Situated between the South China Block and the Simao Block, the Ailaoshan Belt is a significant component of the Jinshajiang–Ailaoshan tectonic-magmatic-metallogenic belt of southwestern China. The formation of the Ailaoshan Belt is closely related to the evolution of the Palaeo-Tethys Ocean. In this study, we constrain ages of sedimentation in the Jinchang Au–Ni deposit in the Ailaoshan Belt, using laser ablation inductively coupled plasma mass spectrometry (LA-ICP-MS) U–Pb ages of the youngest populations of detrital zircons separated from a chert layer and two uncomfortably overlying meta-sandstones. The combined data of the meta-sandstone samples from the Yiwanshui Formation yielded a concordant age of 250.8 ± 0.6 Ma (mean square weighted deviation (MSWD), 2.8; $n = 26$). The chert sample from the Jinchangyan Formation yielded a concordant age of 347.0 ± 1.5 Ma (MSWD, 2.8; $n = 16$). Detrital zircons from the meta-sandstone are characterized by low rare earth element contents (ΣREE) and low Y, and high U and U/Yb ratio, suggesting a continental crustal origin. Zircons in the meta-sandstones were derived mainly from pre-collision subduction zone magmatic rocks related to the closure of the Palaeo-Tethys Ocean. In contrast, detrital zircons from the chert contain relatively high ΣREE and Y, and low U and U/Yb ratio, suggesting an oceanic crust origin. Zircons in the chert bed were derived mainly from ophiolites related to seafloor spreading in a branch of the Palaeo-Tethys Ocean.

1. Introduction

The Ailaoshan tectono-magmatic-metallogenic belt (abbreviated as the Ailaoshan Belt) of southwestern China, along with its northwestern extension in the Jinshajiang Belt, is a significant component of the expansive Tethyan–Himalayan domain (e.g. Allegre *et al.* 1984; Sengör, 1987; Zhong, 2000; Zi *et al.* 2012*a*; Deng *et al.* 2014). This belt contains volcanic and plutonic rocks and ophiolite mélange zones that extend from northeastern Tibet to the eastern Indochina Block (Lai *et al.* 2014*a*, *b*; Fig. 1a). The ophiolite mélange represents a suture zone that has been suggested to be the boundary between the South China Block and the Simao Block that were present within the Palaeo-Tethys Ocean (Chung *et al.* 1997; Sone & Metcalfe, 2008; Jian *et al.* 2009*a*, *b*; Wang *et al.* 2014). Based on palaeontological and geochronological investigations, Zhong (2000), Pan *et al.* (2003) and Liu *et al.* (2008) suggested that the Simao Block now bounded to the east with the Ailaoshan Belt was once a segment of the South China Block. In contrast, recent comprehensive studies of detrital zircon ages and Hf isotope compositions suggest that the Simao Block was derived from the Indochina Block (Wang *et al.* 2014; Yang *et al.* 2018). As a branch of the Palaeo-Tethys, the Ailaoshan Ocean between the South China Block and the Simao Block was in existence during Late Devonian – Early Carboniferous time (Wang *et al.* 2000; Pan *et al.* 2003) and became extinct by subduction during early–late Permian time (Jian *et al.* 2009*b*; Zi *et al.* 2012*b*). However, it is difficult to determine the precise timing and geometry of the suture due to structural complications caused by the collision of India with Asia in Cenozoic time. In particular, provenances and sedimentary ages of widespread Phanerozoic strata in the Ailaoshan Belt are still not clearly confirmed, making reconstruction of the Palaeo-Tethys evolution history still obscure. For example, the Jinchangyan Formation, which is the main host of Au mineralization in the Jichang Au–Ni deposit, has been regarded as Silurian or Devonian with large uncertainties (Internal Exploration Report, 1982; Xiong, 2014). Although several studies focused on magmatic geochronology in this belt and its links with the evolution of the Ailaoshan Ocean (e.g. Zi *et al.* 2012*a*, *c*; Wu *et al.* 2017; Xu *et al.* 2020*a*), there are limited studies focusing on the sediments
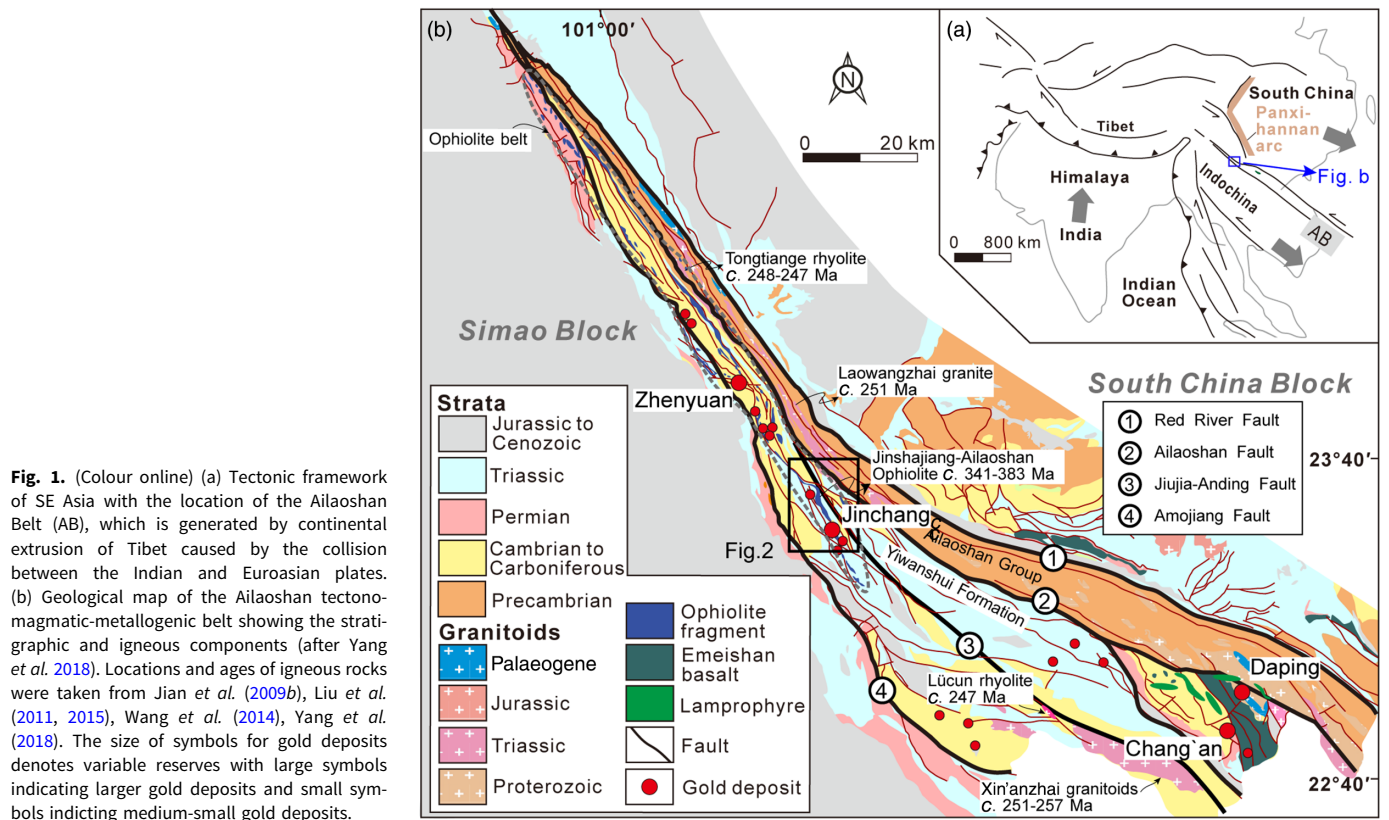
Fig. 1. (Colour online) (a) Tectonic framework of the Ailaoshan Belt (AB), which is generated by continental extrusion of Tibet caused by the collision between the Indian and Euroasian plates. (b) Geological map of the Ailaoshan tectono-magmatic-metallogenic belt showing the stratigraphic and igneous components (after Yang et al. 2018). Locations and ages of igneous rocks were taken from Jian et al. (2009b), Liu et al. (2011, 2015), Wang et al. (2014), Yang et al. (2018). The size of symbols for gold deposits denotes variable reserves with large symbols indicating larger gold deposits and small symbols indicting medium-small gold deposits.

in the belt and their connections between source, transportation pathway and sink basin. A detailed provenance study of the sediments in the Ailaoshan Belt would therefore be helpful to identify the initial source and how these materials were transported. These factors are fundamental for reconstructing the evolution of the Ailaoshan Ocean, a branch of the Palaeo-Tethys Ocean. In addition, a geochronological study of the auriferous strata would help to better constrain mineralization processes.

In this study, we report U–Pb ages and trace-element contents for detrital zircons extracted from the Au-mineralized chert and unconformably overlying meta-sandstones of the Jinchang mining district in the Ailaoshan Belt. Due to widespread distribution of the chert and the meta-sandstone strata in the Ailaoshan Belt, a provenance study of these formations is ideal for revealing the evolution of the Ailaoshan Ocean. In combination with previously reported data, our results improve the understanding of sediment provenance for the studied units and give new insights into the geodynamic setting and evolution of the Palaeo-Tethys.

2. Geological background

The Ailaoshan Belt connects the Jinshajiang suture to the NW and the Song Ma suture to the SE with extension into northern Vietnam (Metcalfe, 2006; Fan et al. 2010). The belt is about 500 km long and 20–100 km wide, and is thought to be the suture that separates the South China Block to the NE from the Simao Block to the SW (Fig. 1a); it is characterized by ophiolitic relics of mafic and ultramafic rocks (Leloup et al. 1995; Jian et al. 2009a, b; Lai et al. 2014a, b; Wang et al. 2014). Deep-penetrating NW-trending faults with moderate to steep dips (60–80° NE; Red River, Ailaoshan, Jiujia–Anding Amojiang faults) cut the belt.

The faults are tightly clustered in the NW and divergent toward the SE (Fig. 1b).

The Proterozoic Ailaoshan Group lies between the Red River and Ailaoshan faults. The group is composed of upper greenschist- to lower amphibolite-grade metamorphic rocks with a total thickness of more than 10 km. Lithologies include gneiss, amphibolite, marble and schist that have yielded whole-rock Rb–Sr ages of 1000–1700 Ma (Yunnan Bureau of Geology and Mineral Resources, 1982). Formation of strata between the Ailaoshan and Jiujia–Anding faults is related to the collision of India and Eurasia during Cenozoic time and the lateral extrusion of the Indochina Block. Offsets of Permian–Triassic flood basalt successions and late Palaeogene highly potassic mafic magmatic rocks imply c. 600 km of left-lateral movement along the belt (Chung et al. 1997). Gold mineralization occurs between the Ailaoshan Fault and the Amojiang Fault. The Ailaoshan Fault separates the Ailaoshan Group metamorphic rocks to the east and Palaeozoic low-grade metamorphic rocks (including Yiwanshui and Jinchangyan formations) and volcanic rocks to the west. The Ailaoshan Belt is bounded on the west by the Simao Block, which is considered part of the Indochina Block (Wang et al. 2014). The basement of the Simao Block is mainly Precambrian high-grade metamorphic rocks (Zhong, 2000). The basement rock is overlain by thick Palaeozoic–Mesozoic sequences of low metamorphic grade. The oldest sedimentary rocks are Lower Ordovician slates, quartzites, marbles and phyllites, which are unconformably overlain by Middle Devonian – Middle Triassic shallow-marine clastic rocks and carbonates (Pan et al. 2003). The Ailaoshan Belt was bounded on the east by the South China Block by the Late Triassic Epoch (Zi et al. 2013). The Permian Emeishan Large Igneous Province extends over the western South China Block to the Jinshajiang–Ailaoshan suture.

The Jinchang Au–Ni deposit is located *c*. 10 km NE of Mojiang County near the Jiujia–Anding fault in the middle portion of the Ailaoshan Belt. The deposit consists of five ore blocks (from NW to SE): Sishibaliangshan, Laojinniu, Lanshan, Pingpo and Mobiliangzi (Xu *et al*. 2020*b*). The eastern segment of the Jinchang deposit is contained in the Jinchang intrusion (387–374 Ma, Jian *et al*. 2009*b*), which consists of peridotites, gabbros, diabase and plagiogranite (Mo *et al*. 1993). Wang *et al*. (2019) suggested that the Jinchang Au–Ni deposit is an orogenic gold deposit. Based on pyrite trace-element composition and *in situ* sulphur isotope, Xu *et al*. (2020*b*) suggested that the ore-forming fluids and metals were dominantly derived from the Jinchang ultramafic intrusion. The western segment is contained in the Triassic Yiwanshui Formation and low-grade metasedimentary rocks of the Jinchangyan Formation. The stratigraphy in the region has been inverted due to folding, with the Triassic Yiwanshui Formation unconformably overlain by the older Jinchangyan Formation. Both units were intruded by the Jinchang ultramafic intrusion (Xu *et al*. 2020*b*).

The Yiwanshui Formation consists of two members with a total thickness of more than 400 m. The upper member consists of sandstone red beds and grey–black siltstone with mudstone interlayers, in which occurs Lamellibranchia and plant fragment fossils (Internal Exploration Report, 1982). The lower member varies in thickness from metres to tens of metres and dominantly occurs in the west segment of the Jinchang mining district. Lithologies of the lower member include meta-sandstone, mudstone and conglomerate-bearing mudstone. The meta-sandstone is grey in colour and has a massive texture. Conglomerate-bearing mudstone occurs at the bottom of the lower member. Conglomerates are dominantly slate, chert and mafic rocks with diameter generally less than 1–2 cm.

The Jinchangyan Formation occurs as a NW-trending succession in the district with a thickness of 100–400 m (Fig. 2). The depositional age of the succession is uncertain due to the lack of geochronological work and the strong deformation in the region, but has been suggested on the basis of palaeontology to be early–middle Silurian (Internal Exploration Report, 1982). However, based on regional stratigraphic correlations, Xiong (2014) proposed that the Jinchangyan Formation is of Devonian age. The formation consists of carbonaceous slate, chert, meta-sandstone, pebble-bearing sandstone, with minor mudstone, greenschist and tuffaceous sandstone. Carbonaceous slate and chert are the main hosts of the Au mineralization.

Three members have been identified for the Jinchangyan Formation. The lower member consists predominantly of dark-grey chert and discontinuous lenticular meta-sandstone beds commonly interbedded with carbonaceous slate. Weak silicification resulted from low-grade regional metamorphism and from subsequent hydrothermal overprinting. Chert is one of the most important hosts for Au mineralization and commonly crops out as cliffs due to the fact that it is highly resistant to weathering. There are two interpretations for the formation of chert in the Jinchangyan Formation: (1) hydrothermal alteration of clastic rocks; or (2) chemical sedimentation following felsic seafloor volcanism. The latter is favoured by Fang *et al*. (2001) and Xie *et al*. (2001). The middle member consists of carbonaceous slate and meta-sandstone, with locally interbedded slate. The middle member is bracketed by a lower discontinuous greenschist bed and an upper limestone bed. No gold mineralization is found in this member, but weak Ni mineralization related to ultramafic intrusions is present. The upper member consists mainly of

carbonaceous slate with calcareous slate interbeds, and lenticular bodies of granite porphyry. Neither Au nor Ni mineralization has been identified in this unit. Contacts between the three members appear to be conformable, but the unit is inverted due to isoclinal folding.

3. Sample descriptions

The Yiwanshui and Jinchangyan formations are widespread in the Ailaoshan Belt. Sedimentary age and provenance studies therefore potentially reveal the evolutionary history of the Ailaoshan Belt, and ultimately the Palaeo-Tethys Ocean. Two samples of meta-sandstone (LS-1 and LS-3) were obtained from outcrops of the Yiwanshui Formation within the Lanshan ore Block (23° 30′ 25″ N, 101° 45′ 11″ E). The *c*. 20 kg samples were taken from the same stratigraphic level but from sites separated by *c*. 15 m laterally. The outcrops were strongly weathered and showed abundant Fe oxyhydroxides (Fig. 3a); removal of weathered surfaces revealed a rock that was massive (LS-1) to laminated (LS-3) and grey in colour (Fig. 3b). Both samples consisted mainly of quartz (70–85%) and sericite (15–30%). Quartz was present as a coarser fraction (50–200 μm grains) set in a matrix of finer quartz (10–20 μm grains) and sericite. Sericite also occurred in 100–300 μm diameter masses pseudomorphing original coarse muscovite crystals.

A single sample of auriferous chert (LS-52) was collected from the lower member of the Jinchangyan Formation within the Lanshan ore block *c*. 50 m NE of the sample location of LS-1. The chert layers are typically strongly fractured, whereas the carbonaceous slate layers are unfractured, reflecting more ductile behaviour during deformation (Fig. 3e). Quartz makes up > 95% of the chert layer with minor amounts of sulphide minerals such as pyrite, pyrrhotite and gersdorffite (Fig. 3f). Quartz grains are typically uniform in size; the sample is characterized by a massive texture.

4. Analytical method and strategy

Samples were crushed to 60–80 mesh for zircon selection. To avoid potential contamination from interbedded slate, we collected the chert sample from a *c*. 50-cm-thick chert layer, and only chert from the middle of the layer was used (Fig. 3e). Because the chert is much harder than the slate, it is easy to wash away slate powders from chert. Zircon grains were separated by conventional heavy liquid and magnetic techniques followed by handpicking under a binocular microscope at the Research Center for Geoanalysis, Hebei Province. Approximately 150, 200 and 150 zircons were collected from LS-1, LS-3 and LS-52, respectively. Zircon grains without cracks and fluid inclusions were mounted onto double-sided adhesive tape and enclosed in an epoxy resin disc that was then polished to expose the crystals. The zircons were photographed under transmitted and reflected light, then internal structures were examined using cathodoluminescence (CL) images obtained with an EMPA-JXA-8100 scanning electron microscope at the Beijing GeoAnalysis Co. Ltd. U–Pb isotope data were obtained by laser ablation inductively coupled plasma mass spectrometry (LA-ICP-MS) at the Nanjing FocuMS Technology Co. Ltd. using an Agilent 7700X equipped with an ASI RESOlution S-155 193 nm excimer ArF laser ablation system. Zircons analysed were selected at random. The analytical procedures and instrument conditions are described in Xie *et al*. (2008) and summarized here. Each acquisition incorporated 20 s background (gas blank) and 40 s sample signals with laser ablation. The laser beam had a repetition
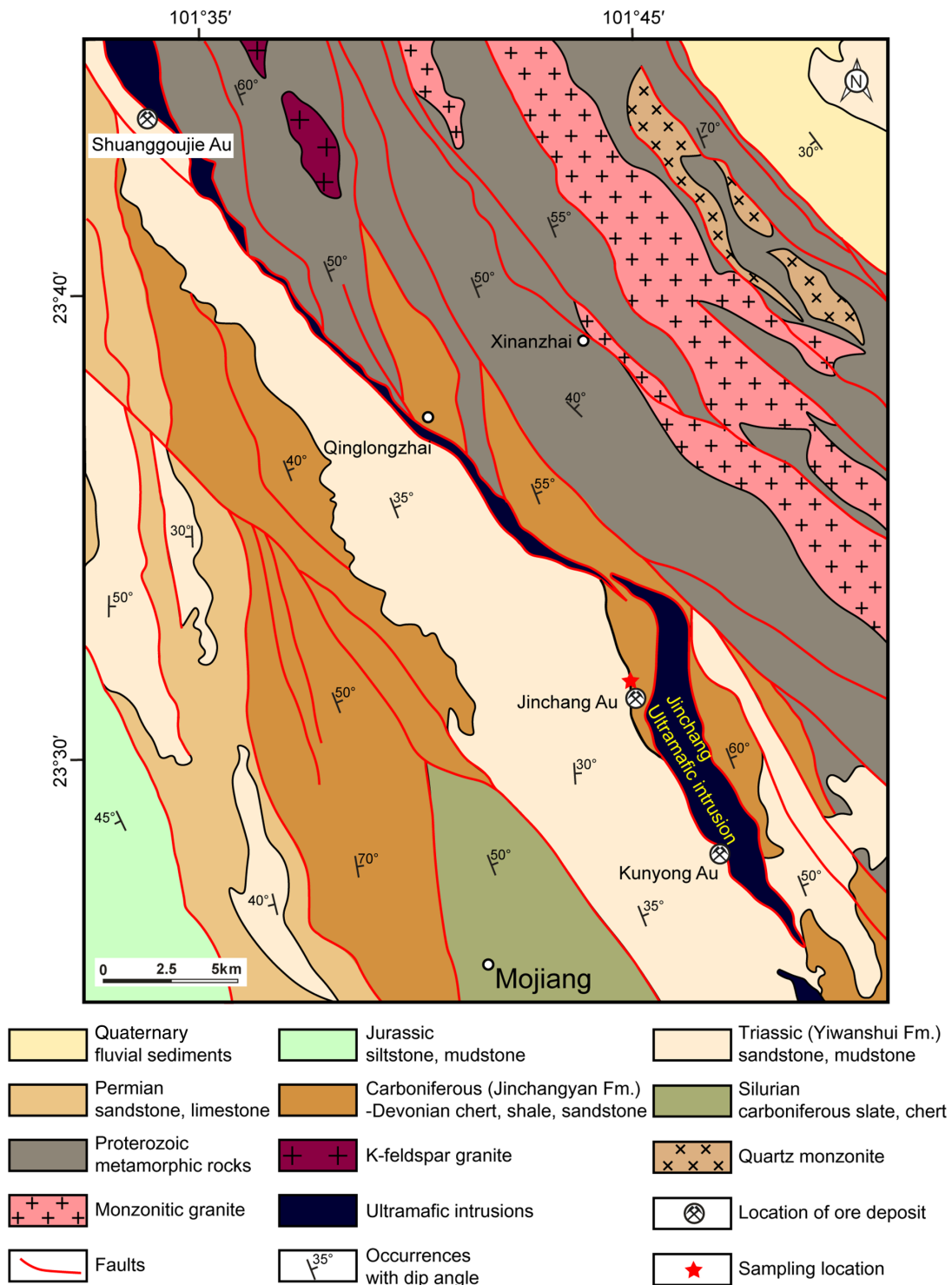
Fig. 2. (Colour online) Geological map of the Jinchang Au–Ni deposit in Mojiang County, the northern segment of the Ailaoshan Belt (modified after 1:20 000 Geological Map of Mojiang sheet, F-47-VI, 1976).

rate of 10 Hz and a spot diameter of *c.* 30 μm. Helium was applied as carrier gas to efficiently transport aerosol out of the ablation cell, and was mixed with argon via a T-connector before entering an ICP torch. Dwell times were set to 20 ms for ^{207}Pb, 15 ms for ^{206}Pb and ^{208}Pb, 10 ms for ^{232}Th and ^{238}U, and 8 ms for other elements. The fractionation correction was performed using the program ICPMSDataCal 9.7 (Liu *et al.* 2010). Harvard zircon

91500 was used as a calibration standard to correct instrumental mass discrimination. Trace-element concentrations were calculated using GLITTER 4.0 (Macquarie University) and calibrated using ^{29}Si as internal standard, and NIST SRM 610 served as external reference material. After every eight unknown analyses, both standards were analysed to monitor accuracy and precision. ^{204}Pb has a potential isobaric interference from ^{204}Hg; this potential
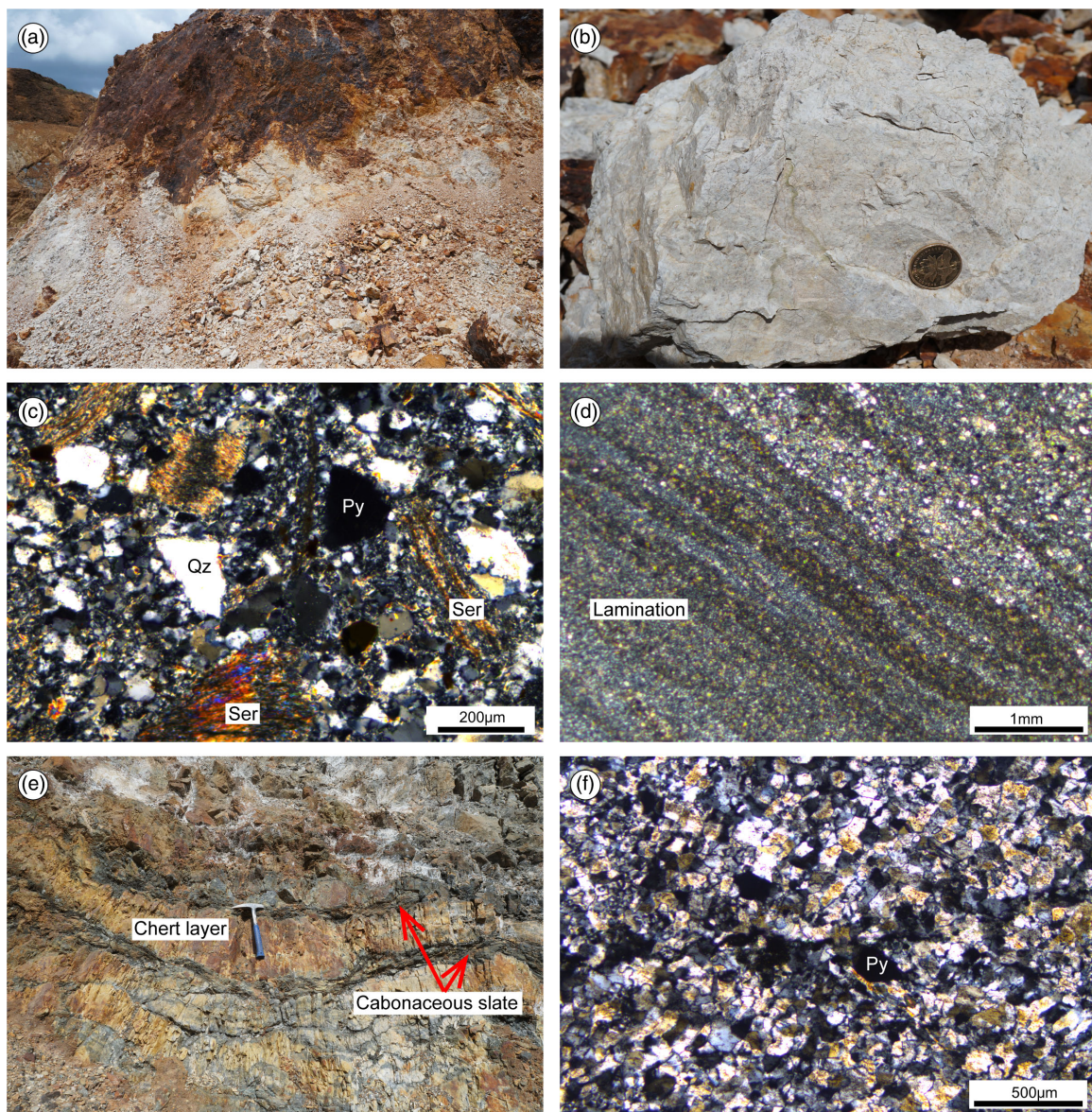
Fig. 3. (Colour online) Field and petrographic photographs of the meta-sandstone and chert samples from the Jinchang Au–Ni mine site examined for detrital zircon analysis. (a) Outcrop of meta-sandstone sampling site showing strong oxidative weathering (LS-1 and LS-3). (b) Hand specimen of sample LS-1, showing that the meta-sandstone sample is grey in colour and has a massive texture. (c) Thin-section petrology for sample LS-1. Coarse anhedral quartz occurs as phenocrysts surrounded by a fine-grained quartz and sericite matrix. The large sericites were altered from muscovite and keep the shape of the original minerals (cross-polarized light). (d) Meta-sandstone (LS-3) consists of fine-grained quartz and muscovite, and occurs as laminated relict texture (cross-polarized light). (e) Sample LS-52 is from a strata-bound Au-mineralized chert (10–30 cm thick), which is interlayered with thin layers of carbonaceous slate (5–20 cm thick). (f) Anhedral quartz is the dominant mineral in the chert, with minor anhedral pyrite intergrown (cross-polarized light). Qz – quartz; Ser – sericite; Py – pyrite.

problem was monitored indirectly by monitoring ^{202}Hg. ^{202}Hg was usually < 10 cps in the gas blank, which indicates that the contribution of ^{204}Hg to ^{204}Pb was negligible. Common Pb was corrected according to the method of Andersen (2002). The weighted mean U–Pb ages and Concordia plots were obtained using ISOPLOT 4.15 (Ludwig, 2010). Errors in individual analyses were based on counting statistics and are reported as 1σ. The U–Pb ages were calculated using U decay constants recommended by Steiger and Jäger (1977), with which the individual analyses all fell within 1σ error at a 95% confidence level.

5. Results

5.a. Zircon U–Pb ages

The U–Pb data for zircons from meta-sandstone samples LS-1 and LS-3 are listed in Table 1. CL images with spot locations and ^{206}Pb/^{238}U ages are shown in Figure 4. The zircons targeted for U–Pb dating generally have clear oscillatory CL zoning and high Th/U ratios (> 0.1), indicating their initial magmatic origin (Allen *et al.* 1998; Rubatto & Gebauer, 2000; Hoskin & Schaltegger, 2003). They are typically transparent, light brown in colour,

Table 1. Zircon LA-ICP-MS U–Pb age data for samples LS-1 and LS-3 from the Jinchang Au–Ni deposit in the northern segment of the Ailaoshan Belt

Spot no.	Concordance (%)	Concentration (ppm)			Th/U	Pb$_C$ (ppm)	Isotope ratios						Calculated apparent age (Ma)					
		Pb$_T$	Th	U			^{207}Pb/^{206}Pb	1σ	^{207}Pb/^{235}U	1σ	^{206}Pb/^{238}U	1σ	^{207}Pb/^{206}Pb	1σ	^{207}Pb/^{235}U	1σ	^{206}Pb/^{238}U	1σ
LS-1																		
91500std	99	21.1	37.5	98.4	0.38	0.30	0.0754	0.0023	1.8673	0.0573	0.1795	0.0023	1079.6	61.1	1069.6	20.3	1064.2	12.7
91500std	99	19.8	34.9	93.1	0.38	0.05	0.0743	0.0024	1.8331	0.0596	0.1788	0.0023	1050.9	66.7	1057.4	21.4	1060.6	12.8
LS-1-01	98	18.7	134	399	0.34	0.54	0.0520	0.0015	0.2917	0.0085	0.0406	0.0005	287.1	64.8	259.9	6.7	256.6	3.0
LS-1-02*	97	20.3	174	224	0.78	1.17	0.0572	0.0023	0.5510	0.0219	0.0697	0.0008	498.2	88.9	445.6	14.3	434.3	4.8
LS-1-03*	99	22.2	224	484	0.46	0.00	0.0516	0.0017	0.2731	0.0087	0.0385	0.0004	264.9	75.9	245.2	6.9	243.8	2.6
LS-1-04	92	14.1	101	311	0.33	1.34	0.0556	0.0019	0.3020	0.0101	0.0394	0.0005	435.2	71.3	268.0	7.9	249.4	3.0
LS-1-05*	92	85.3	314	350	0.90	0.00	0.0827	0.0017	2.0018	0.0467	0.1743	0.0024	1261.1	40.7	1116.1	15.8	1035.9	13.2
LS-1-06	99	15.8	127	340	0.37	0.00	0.0514	0.0020	0.2862	0.0113	0.0404	0.0006	257.5	87.0	255.6	8.9	255.5	3.8
LS-1-07*	91	22.9	229	490	0.47	0.00	0.0560	0.0016	0.3019	0.0086	0.0388	0.0004	453.8	64.8	267.9	6.7	245.6	2.5
LS-1-08*	98	11.1	73.5	128	0.58	0.00	0.0548	0.0022	0.5314	0.0214	0.0703	0.0009	405.6	86.1	432.7	14.2	437.9	5.2
91500std	98	21.1	37.4	99.7	0.37	0.00	0.0726	0.0022	1.8147	0.0567	0.1807	0.0023	1003.4	63.0	1050.8	20.5	1070.9	12.8
91500std	97	20.0	35.5	95.2	0.37	1.77	0.0771	0.0024	1.8857	0.0569	0.1776	0.0022	1125.0	63.0	1076.1	20.0	1053.9	12.0
LS-1-09*	98	64.4	264	423	0.62	0.35	0.0660	0.0014	1.1578	0.0264	0.1262	0.0014	805.6	45.5	780.9	12.4	766.3	8.1
LS-1-10	92	17.0	167	367	0.46	0.53	0.0555	0.0021	0.3018	0.0112	0.0395	0.0005	431.5	89.8	267.8	8.7	249.6	3.2
LS-1-11*	98	50.8	313	197	1.59	0.69	0.0749	0.0017	1.7617	0.0383	0.1702	0.0018	1064.8	46.0	1031.5	14.1	1013.2	9.7
LS-1-12*	96	27.0	104	161	0.65	0.00	0.0694	0.0020	1.3219	0.0431	0.1368	0.0025	922.2	57.4	855.4	18.9	826.8	14.4
LS-1-13*	97	149.5	151	257	0.59	0.00	0.1642	0.0026	10.375	0.1791	0.4538	0.0045	2499.7	26.2	2468.8	16.1	2412.2	20.1
LS-1-14	98	25.9	248	545	0.46	0.00	0.0506	0.0017	0.2833	0.0089	0.0406	0.0005	233.4	75.9	253.3	7.1	256.9	2.9
LS-1-15	97	13.2	98.0	291	0.34	0.03	0.0528	0.0021	0.2915	0.0116	0.0399	0.0005	320.4	90.7	259.7	9.1	252.4	3.0
LS-1-16*	92	31.0	319	652	0.49	0.49	0.0557	0.0016	0.3130	0.0091	0.0408	0.0006	438.9	64.8	276.5	7.0	257.7	3.5
91500std	99	18.9	33.2	90.7	0.37	0.00	0.0747	0.0024	1.8580	0.0603	0.1801	0.0024	1061.1	64.8	1066.3	21.4	1067.6	13.3
91500std	99	18.1	32.6	88.3	0.37	0.14	0.0751	0.0024	1.8424	0.0568	0.1782	0.0024	1070.1	70.5	1060.7	20.3	1057.3	12.9
LS-1-17	99	16.7	135	369	0.37	0.22	0.0517	0.0025	0.2813	0.0129	0.0396	0.0005	272.3	111	251.7	10.2	250.6	3.4
LS-1-18	95	15.7	171	339	0.50	0.00	0.0537	0.0020	0.2903	0.0109	0.0390	0.0005	366.7	54.6	258.8	8.6	246.8	2.9
LS-1-19	99	17.4	136	376	0.36	0.64	0.0514	0.0017	0.2886	0.0093	0.0404	0.0004	257.5	71.3	257.5	7.3	255.2	2.8
LS-1-20	96	20.3	214	428	0.50	0.44	0.0491	0.0017	0.2724	0.0093	0.0401	0.0005	153.8	78.7	244.6	7.5	253.6	2.9
LS-1-21	94	28.4	282	598	0.47	0.00	0.0541	0.0015	0.2991	0.0079	0.0400	0.0004	372.3	63.0	265.7	6.2	252.6	2.5
LS-1-22	98	26.6	339	559	0.61	0.00	0.0504	0.0015	0.2822	0.0093	0.0404	0.0006	213.0	70.4	252.4	7.4	255.2	3.8
LS-1-23*	93	16.7	124	357	0.35	0.00	0.0472	0.0017	0.2716	0.0109	0.0410	0.0006	57.5	85.2	244.0	8.7	259.2	3.6
LS-1-24*	64	11.2	91.0	213	0.43	0.24	0.0781	0.0041	0.4436	0.0224	0.0411	0.0006	1150.0	103.2	372.8	15.7	259.7	3.6

(Continued)

Table 1. (*Continued*)

91500std	98	20.6	36.8	98.8	0.37	0.66	0.0769	0.0023	1.8969	0.0542	0.1787	0.0023	1120.4	65.7	1080.0	19.0	1059.9	12.5
91500std	98	19.8	35.4	94.1	0.38	0.00	0.0728	0.0025	1.8035	0.0572	0.1796	0.0022	1009.3	68.1	1046.7	20.7	1065.0	11.9
LS-3																		
91500std	99	20.8	37.2	99.7	0.37	0.78	0.0749	0.0026	1.8502	0.0589	0.1792	0.0026	1064.8	75.0	1063.5	21.0	1062.4	14.5
91500std	97	20.0	35.8	95.1	0.38	0.00	0.0723	0.0027	1.7698	0.0604	0.1795	0.0025	994.4	74.5	1034.5	22.1	1064.3	13.5
LS-3-01*	99	73.9	138	360	0.38	0.11	0.0746	0.0016	1.8240	0.0391	0.1772	0.0019	1057.4	44.4	1054.1	14.1	1051.7	10.3
LS-3-02	99	28.2	252	612	0.41	0.02	0.0513	0.0015	0.2783	0.0078	0.0395	0.0005	253.8	66.7	249.3	6.2	249.5	2.8
LS-3-03	98	20.0	225	426	0.53	0.00	0.0508	0.0020	0.2784	0.0110	0.0399	0.0005	231.6	88.9	249.4	8.7	252.1	3.3
LS-3-04*	98	72.6	272	546	0.50	0.17	0.0634	0.0013	0.9884	0.0234	0.1128	0.0017	720.4	44.4	697.9	12.0	689.1	9.9
LS-3-05	96	19.4	173	410	0.42	0.40	0.0496	0.0017	0.2769	0.0095	0.0405	0.0005	176.0	77.8	248.2	7.6	255.9	2.8
LS-3-06*	92	249	75.8	834	0.09	0.00	0.1117	0.0024	4.3654	0.1450	0.2772	0.0046	1827.5	39.2	1705.8	27.5	1577.0	23.4
LS-3-07	99	18.2	184	404	0.45	0.54	0.0519	0.0021	0.2792	0.0109	0.0395	0.0005	279.7	94.4	250.0	8.7	250.0	3.4
LS-3-08*	98	51.3	643	603	1.07	0.35	0.0556	0.0014	0.4857	0.0127	0.0634	0.0007	435.2	62.0	402.0	8.7	396.5	4.2
91500std	99	18.8	34.3	91.8	0.37	0.89	0.0751	0.0023	1.8270	0.0560	0.1768	0.0024	1072.2	61.1	1055.2	20.1	1049.7	13.2
91500std	99	20.1	36.0	96.2	0.37	0.45	0.0747	0.0021	1.8734	0.0573	0.1815	0.0025	1061.1	52.8	1071.7	20.3	1075.2	13.7
LS-3-09	99	44.2	276	1036	0.27	0.00	0.0513	0.0016	0.2737	0.0085	0.0387	0.0005	253.8	65.7	245.6	6.8	244.9	3.2
LS-3-10	98	14.6	120	327	0.37	0.00	0.0521	0.0018	0.2800	0.0101	0.0390	0.0004	300.1	81.5	250.6	8.0	246.7	2.8
LS-3-11*	97	24.1	41.7	37.3	1.12	0.58	0.1478	0.0044	9.2079	0.2523	0.4549	0.0073	2320.7	51.7	2358.9	25.1	2416.8	32.5
LS-3-12*	97	26.2	214	295	0.73	0.00	0.0545	0.0016	0.5388	0.0152	0.0721	0.0008	390.8	64.8	437.7	10.0	448.6	5.0
LS-3-13	99	26.6	314	583	0.54	0.00	0.0518	0.0016	0.2762	0.0080	0.0389	0.0005	276.0	65.7	247.6	6.4	246.1	2.8
LS-3-14	96	10.3	86.4	232	0.37	0.00	0.0543	0.0026	0.2863	0.0122	0.0389	0.0005	383.4	106	255.6	9.6	245.8	3.4
LS-3-15	99	29.8	226	659	0.34	0.91	0.0519	0.0014	0.2875	0.0082	0.0403	0.0005	279.7	63.0	256.6	6.5	254.6	3.1
LS-3-16	97	23.1	217	504	0.43	0.73	0.0499	0.0018	0.2714	0.0096	0.0395	0.0005	190.8	83.3	243.8	7.7	249.7	2.9
91500std	99	19.2	34.0	92.1	0.37	0.00	0.0750	0.0024	1.8681	0.0613	0.1802	0.0026	1133.3	64.1	1069.9	21.7	1068.2	14.2
91500std	99	19.8	35.6	96.3	0.37	0.07	0.0748	0.0024	1.8323	0.0590	0.1781	0.0023	1062.7	66.2	1057.1	21.2	1056.6	12.4
LS-3-17*	97	20.2	186	222	0.84	1.55	0.0571	0.0019	0.5497	0.0180	0.0699	0.0008	494.5	74.1	444.8	11.8	435.6	5.0
LS-3-18*	96	71.7	77.3	565	0.14	0.00	0.0665	0.0016	1.0993	0.0300	0.1190	0.0017	820.4	48.9	753.0	14.5	724.6	9.7
LS-3-19	99	24.4	257	524	0.49	0.51	0.0517	0.0016	0.2795	0.0085	0.0392	0.0005	272.3	65.7	250.3	6.8	248.0	2.9
LS-3-20	98	16.4	133	371	0.36	0.00	0.0526	0.0019	0.2788	0.0095	0.0388	0.0005	309.3	79.6	249.7	7.5	245.2	2.8
LS-3-21	99	24.3	218	528	0.41	0.00	0.0511	0.0015	0.2791	0.0080	0.0394	0.0004	255.6	66.7	249.9	6.4	249.1	2.5
LS-3-22*	96	35.3	419	446	0.94	0.00	0.0565	0.0014	0.4668	0.0115	0.0597	0.0006	472.3	53.7	389.0	8.0	373.8	3.6
LS-3-23*	99	89.1	49.3	230	0.21	0.00	0.1145	0.0022	5.2959	0.0994	0.3339	0.0033	1871.9	33.5	1868.2	16.1	1857.1	15.9
LS-3-24	98	22.2	190	488	0.39	0.00	0.0504	0.0019	0.2778	0.0103	0.0398	0.0005	213.0	87.0	248.9	8.2	251.6	2.9
91500std	98	18.7	32.6	90.2	0.36	0.00	0.0763	0.0027	1.8716	0.0639	0.1781	0.0023	1103.4	70.4	1071.1	22.6	1056.7	12.6
91500std	98	17.9	31.1	85.6	0.36	1.59	0.0734	0.0027	1.8288	0.0662	0.1802	0.0025	1027.8	74.1	1055.8	23.8	1068.2	13.5

Note: Pb_T and Pb_C denote the total and common portions, respectively; *indicates that the data are not used for concordant age calculation.
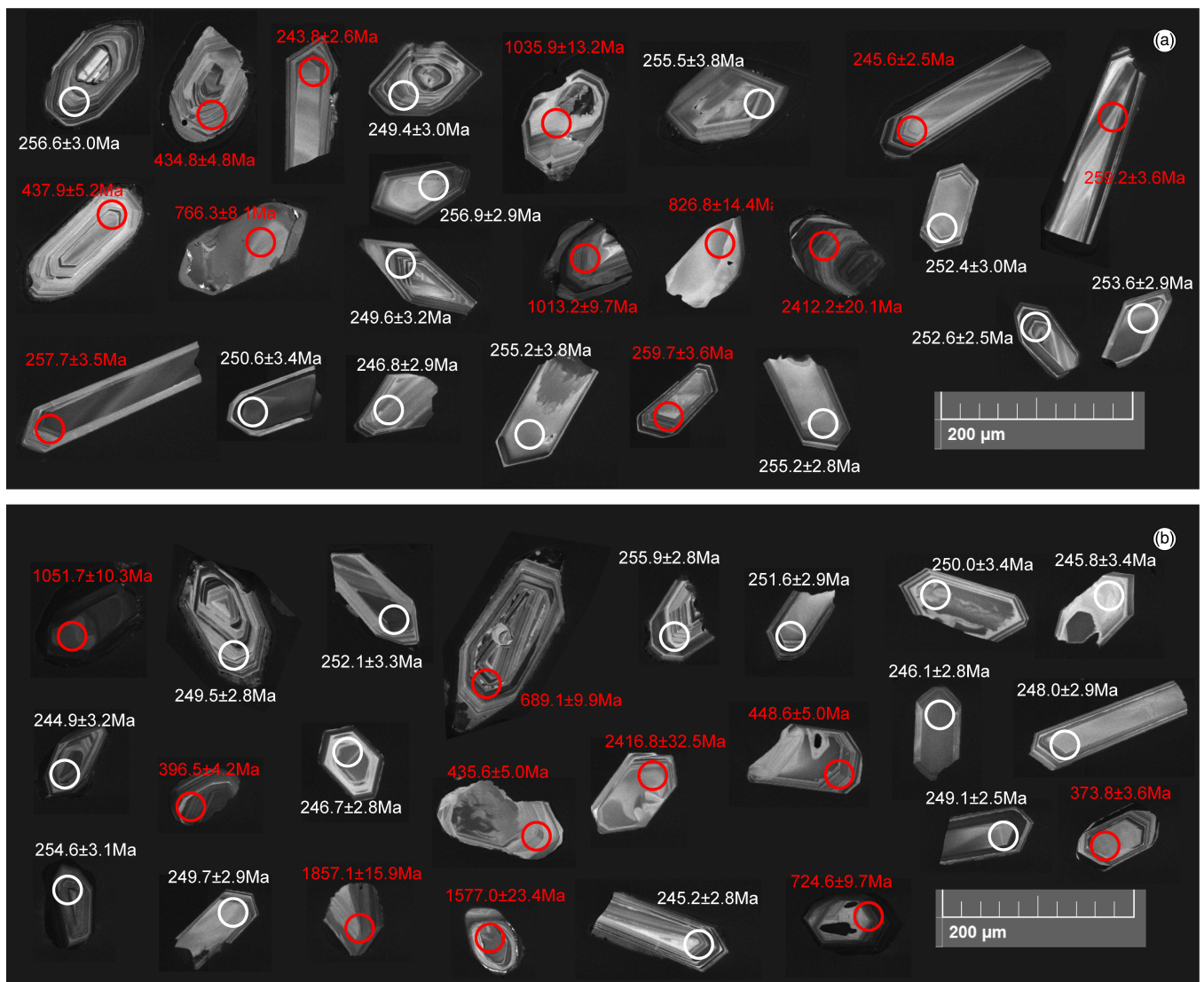
Fig. 4. (Colour online) Cathodoluminescence (CL) images of zircons with [206]Pb/[238]U ages used for U–Pb dating extracted from the meta-sandstone sample (a) LS-1 and (b) LS-3. Circles denote the location of laser ablation. Zircons with white circles are used for the concordant U–Pb age calculation.

100–200 μm in length and 50–100 μm in width (Fig. 4). A large proportion of zircons are excluded from analysis due to their fracture texture or dark colour, indicating strong Pb loss. As a result, only 24 analyses were performed for each sample. Among them, data with discordance rate lower than 95% are not used for concordant age calculation.

Except for one discordant analysis (LS1-24), all zircons from LS-1 contained 128–652 ppm U and 73.5–339 ppm Th, with Th/U ratios varying from 0.33 to 1.59. A total of 16 analyses yielded [206]Pb/[238]U ages of 243.8–259.2 Ma, interpreted as the youngest age population. When four disconcordant ages (LS-1-3, -7, -16 and -23) were disregarded, a concordant age of 252.8 ± 0.9 Ma (mean square weighted deviation (MSWD), 5.3; $n = 12$) (Fig. 5a) is interpreted. Seven analyses of older zircons (LS-1-2, -5, -8, -9, -11, -12 and -13) yielded [206]Pb/[238]U ages older than 400 Ma. CL images of zircons with older ages are either brighter or darker and commonly anhedral in shape (Fig. 4). Although not exclusive, the CL images still offer alternative support to distinguish the older zircons from the younger group.

The U and Th concentrations of zircons from sample LS-3 vary from 37.3 to 1036 ppm and from 41.7 to 643 ppm, respectively,

with Th/U ratios of 0.09–1.19. A total of 14 analyses yielded [206]Pb/[238]U ages of 244.9–255.9 Ma, judged to be the youngest population in the sample. Taking this population gives a concordant age of 249.2 ± 0.8 Ma (MSWD, 0.06; $n = 14$) (Fig. 5b). Ten analyses of this sample (LS-3-1, -4, -6, -8, -11, -12, -17, -18, -22 and -23) yielded much older ages. CL images of these zircons have a dark-grey colour, distinguishing zircons with younger ages that are consistently light-grey in colour (Fig. 4). Because samples LS-1 and LS-3 are stratigraphically equivalent, it is reasonable to combine the data to obtain a more precise age. The grouped data yield a concordant age of 250.8 ± 0.6 Ma (MSWD, 2.8; $n = 26$) (Fig. 5c), which can be considered the maximum depositional age for the Yiwanshui Formation.

The U–Pb data of zircons from the chert sample (LS-52) are listed in Table 2. CL images with spot locations and [206]Pb/[238]U ages are shown in Figure 6. In contrast with the zircons from the meta-sandstone which are euhedral, zircons from the chert sample are mostly rounded, suggesting significant transport. In addition, zircon size is variable ranging from 60 to 200 μm in diameter. The analysed zircons are bright-grey to dark-grey in colour, and
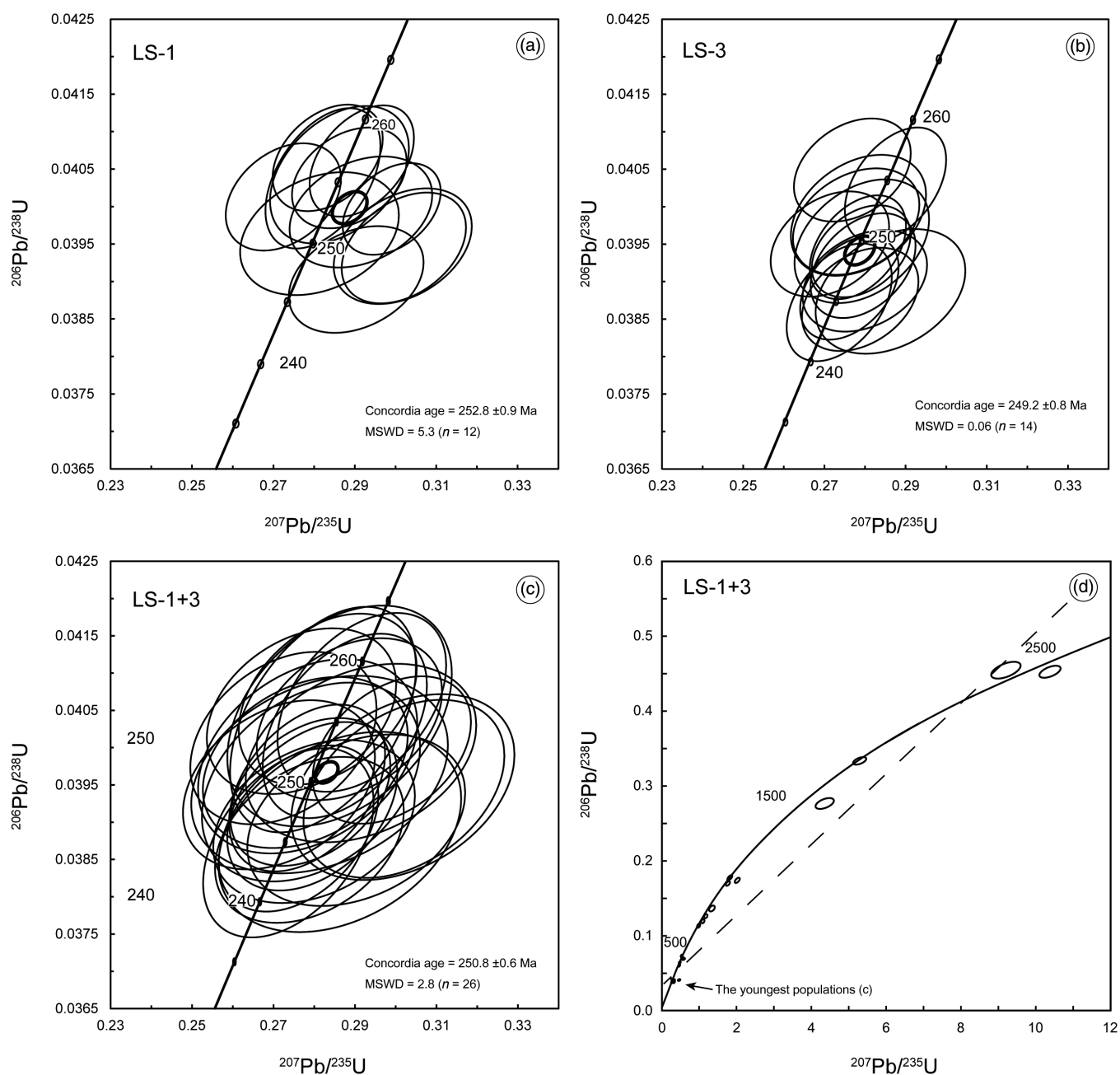
Fig. 5. (Colour online) Zircon U–Pb Concordia diagrams for the zircons with youngest populations from the meta-sandstone (a) LS-1, (b) LS-3 and (c) joint LS-1+3, as well as (d) all zircons analysed from LS-1+3.

most lack zonation (Fig. 6). We omitted four analyses (LS-52-06, -11, -15 and -17) due to poor concordance. The remaining zircons contain 14.5–374 ppm U and 9.79–283 ppm Th, with Th/U ratios varying from 0.41 to 1.25. These results imply that the zircons are of magmatic origin. Another four analyses are disconcordant and yielded either much older or much younger ages (LS-52-20, -21, -22 and -24). CL images of these zircons are much darker than other zircons (Fig. 6). The remaining 16 analyses yielded $^{206}Pb/^{238}U$ ages of 343.7–354.1 Ma, with a concordant age of 347.0 ± 1.5 Ma (MSWD, 0.11) (Fig. 7), which can be considered a maximum age for sedimentation of the chert layer.

5.b. Trace-element compositions

The trace-element compositions of zircons used for concordant age calculation are listed in Table 3. Rare earth element (REE) patterns for the meta-sandstone zircons are similar to those for the chert layer zircons. Both exhibit enrichment in heavy REEs (HREEs), positive Ce anomalies and negative Eu anomalies (Fig. 8). The total REE concentrations of the meta-sandstone zircons vary from 1287 to 3551 ppm (mean, 2265 ppm), which is much lower than the concentrations in the chert zircons of 3759–14 315 ppm (mean, 8848 ppm).

Table 2. Zircon LA-ICP-MS U–Pb age data for sample LS-52 from the Jinchang Au–Ni deposit in the northern segment of the Ailaoshan Belt

Spot no.	Concordance (%)	Concentration (ppm)			Th/ U	Pb$_C$ (ppm)	Isotope ratios						Calculated apparent age (Ma)					
		Pb$_T$	Th	U			$^{207}Pb/$ ^{206}Pb	1σ	$^{207}Pb/$ ^{235}U	1σ	$^{206}Pb/$ ^{238}U	1σ	$^{207}Pb/$ ^{206}Pb	1σ	$^{207}Pb/$ ^{235}U	1σ	$^{206}Pb/$ ^{238}U	1σ
91500std	98	18.8	32.7	90.6	0.36	0	0.0766	0.0027	1.8785	0.0639	0.1781	0.0023	1110.2	75.0	1073.5	22.6	1056.8	12.6
91500std	98	18.0	31.3	86.0	0.36	1.61	0.0732	0.0027	1.8219	0.0661	0.1802	0.0025	1020.4	78.7	1053.4	23.8	1068.0	13.5
LS-52-01	94	1.38	13.7	19.7	0.70	0.37	0.0578	0.0045	0.4406	0.0315	0.0559	0.0010	520.4	172.2	370.7	22.2	350.9	6.4
LS-52-02	92	2.79	38.3	36.4	1.05	0.00	0.0583	0.0029	0.4474	0.0226	0.0556	0.0009	542.6	113.9	375.4	15.8	348.8	5.5
LS-52-03	99	2.23	19.7	32.3	0.61	0.12	0.0546	0.0036	0.4075	0.0264	0.0556	0.0009	394.5	150.0	347.1	19.0	349.1	5.7
LS-52-04	95	2.56	33.6	34.1	0.99	0.23	0.0579	0.0035	0.4314	0.0245	0.0557	0.0010	527.8	131.5	364.2	17.4	349.3	6.4
LS-52-05	99	3.71	59.3	47.5	1.25	0.00	0.0543	0.0028	0.4039	0.0200	0.0551	0.0008	383.4	116.7	344.5	14.5	345.5	4.6
LS-52-06*	82	20.1	261	753	0.35	1.37	0.0588	0.0013	0.1847	0.0042	0.0227	0.0002	561.1	50.0	172.1	3.6	144.6	1.4
LS-52-07	97	3.05	44.0	39.3	1.12	0.14	0.0521	0.0028	0.3954	0.0204	0.0555	0.0009	300.1	122.2	338.3	14.9	348.2	5.3
LS-52-08	97	2.80	31.0	40.1	0.77	0.00	0.0528	0.0029	0.3941	0.0209	0.0550	0.0008	320.4	125.9	337.4	15.2	345.2	5.0
91500std	99	21.2	38.8	102.0	0.38	0.00	0.0750	0.0022	1.8626	0.0558	0.1798	0.0023	1069.4	59.3	1067.9	19.8	1066.0	12.7
91500std	99	16.7	29.0	80.7	0.36	0.00	0.0747	0.0026	1.8378	0.0630	0.1785	0.0022	1061.1	69.0	1059.1	22.5	1058.8	12.0
LS-52-09	97	1.60	21.4	21.2	1.01	0.21	0.0572	0.0046	0.4191	0.0311	0.0551	0.0011	498.2	205.5	355.4	22.3	346.0	7.0
LS-52-10	96	2.15	20.0	31.7	0.63	0.31	0.0521	0.0036	0.3875	0.0259	0.0548	0.0009	300.1	157.4	332.5	19.0	343.7	5.8
LS-52-11*	79	2.79	36.5	34.3	1.06	0.01	0.0714	0.0039	0.5499	0.0270	0.0576	0.0009	968.5	113.0	444.9	17.7	361.2	5.4
LS-52-12	99	3.14	40.4	43.2	0.93	0.00	0.0537	0.0031	0.4026	0.0219	0.0548	0.0007	366.7	123.1	343.5	15.9	344.0	4.5
LS-52-13	97	2.34	21.0	32.7	0.64	0.41	0.0532	0.0036	0.4035	0.0264	0.0565	0.0010	344.5	153.7	344.2	19.1	354.1	6.0
LS-52-14	98	1.50	17.7	21.2	0.84	0.00	0.0584	0.0042	0.4093	0.0236	0.0549	0.0012	542.6	159.2	348.4	17.0	344.4	7.5
LS-52-15*	84	1.04	10.4	14.1	0.74	0.53	0.0674	0.0062	0.5034	0.0422	0.0563	0.0013	850.0	193.7	414.0	28.5	353.1	8.2
LS-52-16	98	2.81	29.3	40.9	0.72	0.00	0.0546	0.0031	0.4093	0.0224	0.0548	0.0009	394.5	127.8	348.4	16.1	344.2	5.3
91500std	99	19.0	34.1	91.6	0.37	0.00	0.0756	0.0024	1.8559	0.0574	0.1779	0.0023	1084.3	63.0	1065.5	20.4	1055.7	12.4
91500std	99	18.3	32.3	86.9	0.37	0.00	0.0742	0.0026	1.8445	0.0635	0.1804	0.0025	1055.6	69.3	1061.5	22.7	1069.1	13.9
LS-52-17*	80	0.71	7.21	10.3	0.70	0.32	0.0920	0.0275	0.5178	0.0528	0.0555	0.0017	1533.3	591.7	423.7	35.3	348.1	10.3
LS-52-18	98	1.86	21.7	26.5	0.82	0.00	0.0528	0.0044	0.3994	0.0315	0.0551	0.0010	316.7	190.7	341.2	22.8	346.0	6.3
LS-52-19	98	1.76	22.3	24.0	0.93	0.57	0.0552	0.0041	0.4000	0.0277	0.0553	0.0010	420.4	173.1	341.7	20.1	346.9	6.3
LS-52-20*	91	1.99	26.6	27.6	0.96	0.06	0.0613	0.0044	0.4319	0.0264	0.0531	0.0010	650.0	153.7	364.5	18.7	333.3	6.3
LS-52-21*	97	14.7	82.2	180	0.46	0.97	0.0570	0.0016	0.5526	0.0147	0.0699	0.0007	500.0	61.1	446.7	9.6	435.6	4.5
LS-52-22*	98	217	283	360	0.79	1.21	0.1578	0.0025	9.7916	0.1589	0.4443	0.0037	2431.8	26.7	2415.4	15.0	2369.7	16.7
LS-52-23	98	1.00	9.79	14.5	0.68	0.20	0.0552	0.0059	0.4213	0.0444	0.0560	0.0015	420.4	247.2	357.0	31.7	351.5	9.4
LS-52-24*	99	17.4	154	374	0.41	0.72	0.0513	0.0018	0.2884	0.0101	0.0406	0.0005	253.8	88.0	257.3	8.0	256.6	3.1
91500std	98	16.5	28.4	79.6	0.36	0.05	0.0742	0.0028	1.8298	0.0640	0.1802	0.0027	1047.8	75.9	1056.2	23.0	1068.1	14.6
91500std	98	18.2	32.8	88.7	0.37	0.00	0.0755	0.0024	1.8706	0.0595	0.1781	0.0025	1083.3	64.8	1070.7	21.0	1056.8	13.7

Note: Pb$_T$ and Pb$_C$ denote the total and common portions, respectively; *indicates that the data are not used for concordant age calculation.
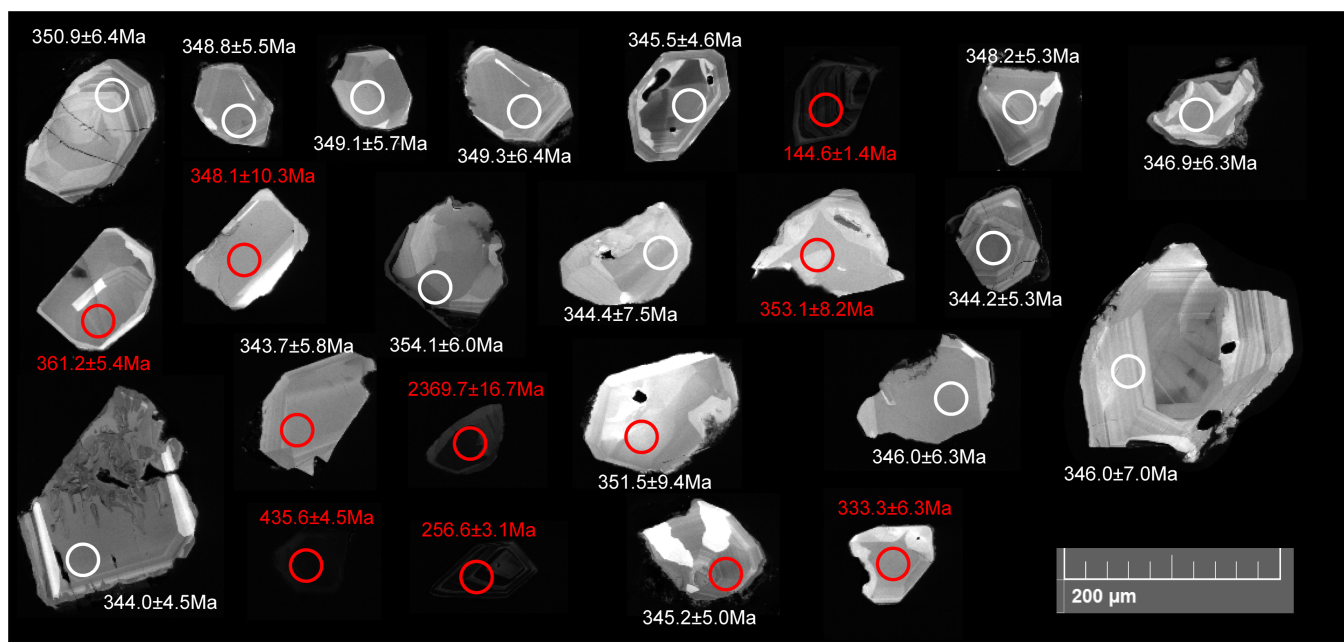
Fig. 6. (Colour online) Cathodoluminescence (CL) images of zircons with [206]Pb/[238]U ages used for U–Pb dating extracted from the chert sample LS-52. Circles denote the location of laser ablation. Zircons with white circles are used for the concordant U–Pb age calculation.
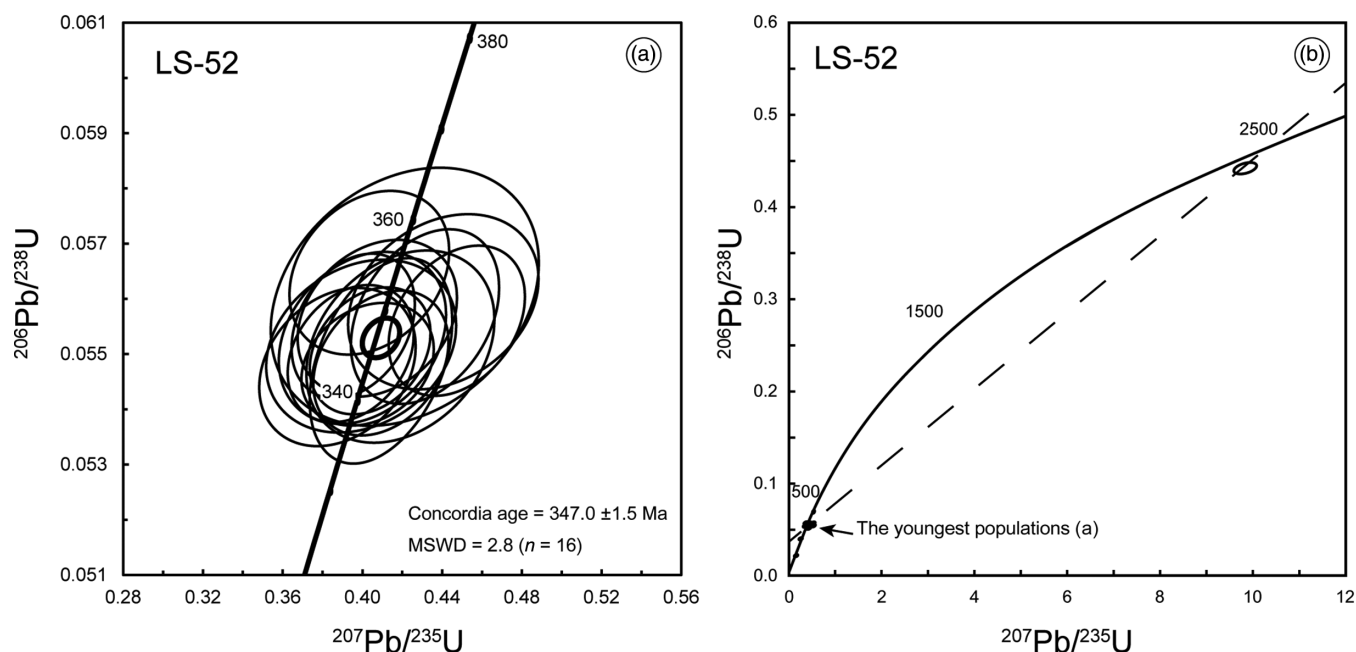
Fig. 7. Zircon U–Pb Concordia diagrams for the zircons with (a) the youngest populations and (b) all zircons from chert sample LS-52.

The uranium (U) concentrations of meta-sandstone zircons vary from 232 to 1036 ppm (mean, 462 ppm). This is one order of magnitude higher than the U concentrations of zircons from the chert sample, which vary from 14.5 to 47.5 ppm (mean, 31.6 ppm). Hafnium (Hf) compositions exhibit similar patterns. The Hf concentration of meta-sandstone zircons varies from 8595 to 10 916 ppm (mean, 9091 ppm), which is slightly higher in general than that of the chert of 7945–9887 ppm (mean, 8664 ppm). In contrast, the ytterbium (Yb) concentration of the

meta-sandstone zircons ranges from 242 to 694 ppm (mean, 406 ppm), much lower than the Yb concentration of the chert zircons, which varies from 765 to 2626 ppm (mean, 1677 ppm). Similar to Yb, phosphorous (P) contents vary from 207 to 785 ppm (mean, 396 ppm) for the meta-sandstone zircons, while the chert sample shows higher contents of 658–2535 ppm (mean, 1520 ppm). The U/Yb ratios of the meta-sandstone zircons are two orders of magnitude higher than the U/Yb ratios of the chert zircons of 0.95–1.82 and 0.012–0.026, respectively. The Nb/Yb

Table 3. Trace-element composition of zircons used for the concordant age calculation from samples LS-1, LS-3 and LS-52

Spot no.	P	Ca	Ti	Nb	Hf	Ta	Pb	Th	U	La	Ce	Pr	Nd	Sm	Eu	Gd	Tb	Dy	Y	Ho	Er	Tm	Yb	Lu	ΣREE	U/Yb	Nb/Yb
LS-1																											
LS-1-01	357		18.6	1.90	9320	0.89	18.7	134	399	0.091	2.41	0.08	1.24	3.42	0.24	19.2	6.62	79.7	895	30.9	137	31.8	296	51.0	1554	1.35	0.006
LS-1-04	275		14.6	1.51	8812	0.71	14.1	101	311	0.002	1.89	0.06	1.11	2.98	0.26	17.1	5.72	68.9	772	26.9	118	27.6	260	45.4	1348	1.19	0.006
LS-1-06	275		14.1	1.66	9029	0.78	15.8	127	340	0.052	2.32	0.07	1.27	3.26	0.29	20.4	7.24	85.8	951	33.1	144	32.6	306	52.3	1640	1.11	0.005
LS-1-10	279		27.1	2.16	8808	0.74	17.0	167	367	0.231	2.83	0.16	2.10	4.49	0.41	26.6	8.91	103	1140	38.6	167	37.5	347	57.3	1935	1.06	0.006
LS-1-14	385		14.6	2.79	8890	1.09	25.9	248	545	0.008	3.57	0.10	1.99	4.78	0.41	28.4	10.0	120	1358	46.5	201	44.8	411	70.0	2301	1.33	0.007
LS-1-15	344		11.8	1.45	8751	0.73	13.2	98.0	291	0.010	1.88	0.06	1.09	2.66	0.33	17.0	6.20	77.4	868	30.3	134	30.7	293	50.9	1513	0.99	0.005
LS-1-17	331	1351	14.6	2.15	8894	0.81	16.7	135	369	0.003	2.46	0.05	1.47	3.47	0.29	21.2	7.59	93.4	1070	37.2	167	38.1	350	63.1	1856	1.05	0.006
LS-1-18	285		10.8	1.17	9069	0.57	15.7	171	339	0.015	2.53	0.19	3.74	8.26	0.58	38.3	11.7	127	1273	45.6	183	40.1	356	59.9	2150	0.95	0.003
LS-1-19	408	242	11.5	1.83	8595	0.88	17.4	136	376	0.014	2.30	0.08	1.63	4.19	0.30	23.7	8.11	95.0	1053	37.1	161	36.5	342	60.5	1826	1.10	0.005
LS-1-20	371		13.2	1.86	8847	0.78	20.3	214	428	0.017	3.01	0.21	3.65	7.77	0.57	40.8	13.0	148	1503	53.1	217	47.8	423	72.9	2535	1.01	0.004
LS-1-21	459		20.0	3.76	8792	1.36	28.4	282	598	0.026	3.94	0.11	2.15	4.94	0.44	36.6	12.8	157	1820	60.4	260	57.6	517	89.8	3023	1.16	0.007
LS-1-22	325		13.7	1.84	8930	0.71	26.6	339	559	0.048	3.77	0.40	6.94	12.8	0.98	63.6	19.7	211	2127	73.1	292	62.0	539	90.1	3502	1.04	0.003
LS-3																											
LS-3-02	785		11.3	4.32	9492	1.49	28.2	252	612	0.422	5.02	0.25	2.63	5.51	0.33	32.0	12.1	157	1836	61.4	269	61.0	560	96.3	3100	1.09	0.008
LS-3-03	351	568	14.6	1.83	8830	0.73	20.0	225	426	0.046	2.99	0.24	4.09	7.77	0.66	40.0	12.7	138	1435	49.6	207	44.8	405	67.3	2415	1.05	0.005
LS-3-05	361	44.3	13.3	2.48	8710	0.87	19.4	173	410	0.006	3.02	0.13	2.26	4.77	0.44	29.1	9.89	117	1278	44.8	190	42.9	395	67.8	2186	1.04	0.006
LS-3-07	296		13.6	1.84	8811	0.86	18.2	184	404	0.008	2.77	0.17	3.16	6.04	0.53	33.5	10.6	127	1343	46.8	195	43.8	396	67.1	2275	1.02	0.005
LS-3-09	555		4.73	8.05	10916	3.45	44.2	276	1036	0.003	5.77	0.06	1.48	3.94	0.41	31.3	12.5	163	2053	68.5	315	73.8	694	128	3551	1.49	0.012
LS-3-10	358	206	13.3	1.70	8761	0.71	14.6	120	327	0.006	2.02	0.07	1.32	3.69	0.27	20.2	7.41	88.1	984	34.2	151	34.7	325	56.5	1708	1.01	0.005
LS-3-13	332		9.73	2.09	9540	0.80	26.6	314	583	0.011	3.90	0.34	6.55	10.8	0.78	57.7	17.6	192	1976	67.6	276	58.8	521	87.6	3277	1.12	0.004
LS-3-14	207		12.7	1.36	9197	0.63	10.3	86.4	232	0.036	2.10	0.09	1.28	3.13	0.28	17.2	5.78	69.0	738	26.1	114	26.6	242	41.8	1287	0.96	0.006
LS-3-15	255	233	2.80	2.09	10875	1.57	29.8	226	659	0.006	5.37	0.04	1.00	2.72	0.24	17.5	6.49	81.3	977	33.0	149	37.1	362	64.0	1736	1.82	0.006
LS-3-16	561	189	12.2	2.78	9062	1.04	23.1	217	504	0.013	3.30	0.10	2.42	6.10	0.43	35.7	12.6	156	1784	60.3	258	56.8	526	90.1	2992	0.96	0.005
LS-3-19	375		14.9	2.99	8874	1.05	24.4	257	524	0.002	3.71	0.12	2.24	6.08	0.48	33.9	11.7	137	1507	52.1	217	48.9	445	75.8	2542	1.18	0.007
LS-3-20	331		15.3	2.21	8720	0.82	16.4	133	371	0.010	2.31	0.05	1.31	3.52	0.30	21.0	7.74	95.8	1108	38.3	167	38.3	360	62.1	1906	1.03	0.006
LS-3-21	416	604	11.2	2.93	9050	1.09	24.3	218	528	0.000	3.19	0.11	1.97	5.40	0.41	29.3	10.2	124	1402	48.3	209	48.8	449	76.9	2409	1.18	0.007
LS-3-24	373	234	16.1	3.12	8801	1.07	22.2	190	488	0.008	2.97	0.10	1.69	4.61	0.34	27.6	9.77	119	1350	46.3	203	45.5	428	72.6	2311	1.14	0.007
LS-52																											
LS-52-01	658		10.8	2.48	9810	1.04	1.38	13.7	19.7	0.05	9.95	0.09	1.83	4.69	1.03	32.0	12.9	171	2155	70.8	332	79.0	765	123	3759	0.026	0.003
LS-52-02	1839	257	42.7	4.17	8197	1.52	2.79	38.3	36.4	0.13	42.9	0.45	8.24	18.6	5.27	123	46.2	586	6702	229	1044	217	2165	302	11490	0.017	0.002
LS-52-03	1052		8.74	5.58	8143	1.75	2.23	19.7	32.3	0.00	18.9	0.15	3.63	10.3	2.50	67.7	26.4	347	4123	141	640	147	1413	220	7161	0.023	0.004
LS-52-04	1777		11.9	3.90	8302	1.56	2.56	33.6	34.1	0.02	42.7	0.35	7.12	17.5	4.90	117	44.3	562	6473	221	1031	212	2114	290	11137	0.016	0.002
LS-52-05	2185	272	13.2	5.03	8176	1.88	3.71	59.3	47.5	0.03	57.3	0.52	10.3	24.8	6.90	156	58.9	738	8369	287	1326	265	2626	389	14315	0.018	0.002

(Continued)

Table 3. (Continued)

LS-52-07	1884		12.7	4.27	8291	1.69	3.05	44.0	39.3	0.01	45.9	0.31	6.77	16.6	4.89	113	43.4	555	6376	218	1008	211	2103	289	10992	0.019	0.002
LS-52-08	2215	85.4	14.5	4.57	9887	1.72	2.80	31.0	40.1	1.64	27.8	0.89	7.26	10.9	1.92	71.6	30.4	418	5430	176	853	199	2127	316	9671	0.019	0.002
LS-52-09	970	232	11.8	2.53	7945	1.11	1.60	21.4	21.2	0.01	24.5	0.13	2.50	7.52	2.59	53.9	21.0	273	3149	109	483	109	1021	155	5411	0.021	0.002
LS-52-10	1163		10.2	5.92	8057	1.86	2.15	20.0	31.7	0.01	23.7	0.16	3.25	9.62	2.52	68.3	27.1	359	4230	147	656	148	1406	217	7298	0.023	0.004
LS-52-12	1902		7.33	3.86	9875	1.63	3.14	40.4	43.2	0.01	40.9	0.28	6.79	19.3	4.19	127	48.2	608	6926	237	1085	224	2208	329	11863	0.020	0.002
LS-52-13	1159		7.64	3.99	8922	1.70	2.34	21.0	32.7	0.05	18.5	0.20	3.99	10.9	2.57	70.6	27.0	349	3988	138	620	142	1358	207	6935	0.024	0.003
LS-52-14	1253	343	10.9	2.93	8451	1.18	1.50	17.7	21.2	0.02	23.5	0.20	4.42	11.5	3.06	71.2	27.5	359	4157	143	642	146	1399	219	7206	0.015	0.002
LS-52-16	2535		8.78	6.01	9058	2.15	2.81	29.3	40.9	1.39	28.1	3.18	41.3	81.0	39.8	307	81.6	767	6693	231	893	180	1714	240	11301	0.024	0.004
LS-52-18	1204		10.8	2.80	8193	1.12	1.86	21.7	26.5	0.01	21.7	0.26	5.76	15.3	4.10	94.2	34.7	431	4797	166	725	160	1551	224	8231	0.017	0.002
LS-52-19	1296		9.95	2.69	8249	1.08	1.76	22.3	24.0	0.02	26.9	0.29	6.02	15.1	4.45	91.3	33.9	435	5070	172	769	171	1690	240	8725	0.014	0.002
LS-52-23	1220	79.8	7.05	2.55	9068	1.18	1.00	9.79	14.5	0.01	23.5	0.11	2.36	7.75	2.39	56.2	22.3	295	3543	119	537	122	1175	170	6077	0.012	0.002

ratios of meta-sandstone zircons vary from 0.003 to 0.153, which is generally higher than the ratios of the chert zircons (0.002–0.004).

6. Discussion

6.a. Detrital zircon U-Pb ages

Detrital zircon geochronology has developed into an essential tool for studies of clastic strata during the past two decades. A basic tenet of detrital zircon geochronology is that a sedimentary unit can be no older than its youngest detrital zircon grains. Hence, the youngest U–Pb age in a population of detrital zircons constrains the maximum depositional age of the host stratigraphic unit (e.g. Stewart *et al.* 2001; Surpless *et al.* 2006; Dickinson & Gehrels, 2009; Gehrels, 2014). This approach is especially useful for dating metamorphosed strata that lack biostratigraphic age controls. However, there are potential complications that can result in measured dates that are younger than the true age of deposition, including Pb loss, poor precision of analysis and uncertainty of the decay constant for ^{238}U (Gehrels, 2014). This bias can be partly accounted for by using the youngest group of ages from a sample after evaluating the possibility of Pb loss using CL images (Dickinson & Gehrels, 2009). In this study, we used concordant U–Pb ages for the youngest group of zircons to constrain the maximum depositional age of the auriferous chert of the Jinchangyan Formation and overlying meta-sandstone of the Yiwanshui Formation in the Jinchang Au deposit. The zircons from meta-sandstone samples LS-1 and LS-3 yielded youngest U–Pb ages of 243.8 ± 2.6 Ma (LS-1-03) and 244.9 ± 3.2 Ma (LS-3-09), which is only slightly younger than the concordant U–Pb ages of 252.8 ± 0.9 Ma and 249.2 ± 0.3 Ma, respectively. The close agreement between the single youngest zircon and the concordant age for each sample supports the conclusion that our concordant U–Pb ages give a robust maximum age of the sedimentary strata. With respect to sample LS-52, the youngest zircon yields a U–Pb age of 144.6 ± 1.4 Ma (LS-52-06) and shows a high degree of discordance compared with the much older concordant U–Pb age of 347.0 ± 1.5 Ma. We interpret the offset between the youngest and the concordant age to result from Pb loss in grain LS-52-06. Zircons LS-52-06, LS-52-21, LS-52-22 and LS-52-24, with a very dark colour in CL images, were omitted from the calculation of the concordant age to avoid inaccuracy due to Pb loss. The concordant age of the youngest zircons from the chert sample constrains the maximum depositional age of Au-bearing chert of 347 Ma. Our new age for the chert sample therefore suggests that the auriferous chert of the Jinchangyan Formation is Early Carboniferous or younger, and not Silurian or Devonian as suggested by previous workers (Internal Exploration Report, 1982; Fang *et al.* 2001; Xiong, 2014).

6.b. Provenance constraints

Most of the *c.* 250 Ma detrital zircons observed in this study have euhedral to subhedral morphology (Fig. 4), implying a short transport distance from their source region. Mesozoic intrusive and volcanic rocks are pervasive along the Ailaoshan Belt. Based on both radiometric and geochemical data, Zi *et al.* (2013) classified magmatic rocks in the Jinshajiang–Ailaoshan Belt into three groups: pre-collision granitoids, syn-collision volcanic rocks and post-collision granitoids. The pre-collision subduction-related magmatism consists mainly of granite, diorite and monzogranite. Zircon U–Pb dating indicates that the pre-collision magmatism occurred during 257–245 Ma, with peak ages at *c.* 250 Ma (Table 4).
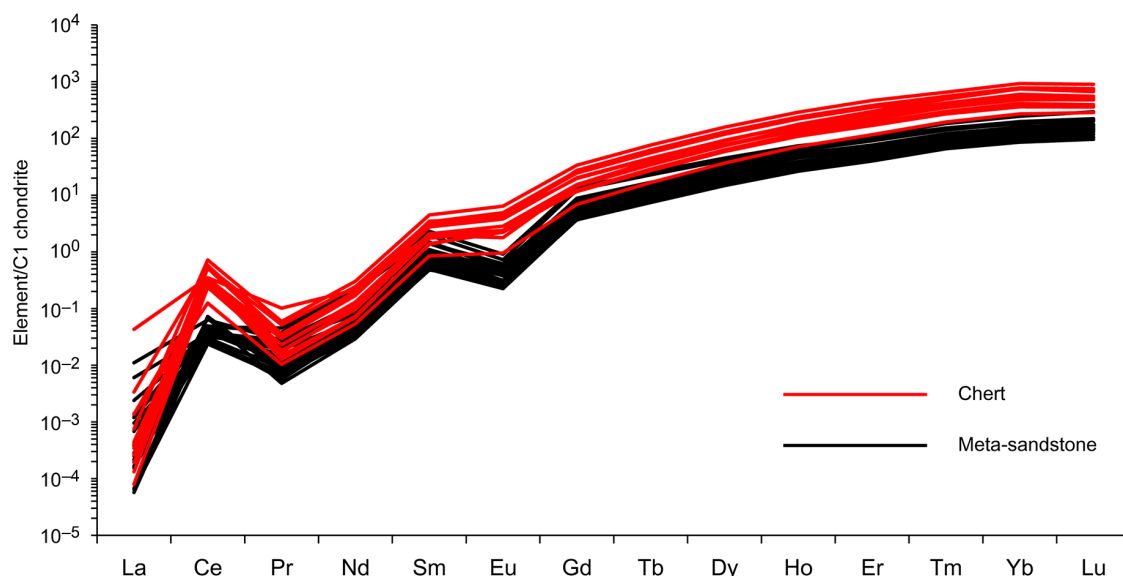
Fig. 8. (Colour online) Rare earth element (REE) concentrations for zircons from the meta-sandstone (black solid lines) and the chert (red solid lines). The REE values are normalized to C1 chondrite (McDonough & Sun, 1995). The distribution pattern is generally similar, with HREE-enriched, positive Ce anomalies and negative Eu anomalies. Total REE contents in zircons from the chert are higher than those from the meta-sandstone.

Examples include the granite dyke at Laowangzhai, c. 80 km NW of the Jinchang deposit, which has a concordant age of 251 ± 1.4 Ma, similar to the Xin'anzhai monzogranite of 251–252 Ma and Baimaxueshan granodiorite and diorite of 248–253 Ma (Zi et al. 2012c; Liu et al. 2015). Syn-collision period is dominated by volcanic rocks, with zircon U–Pb ages varying from 239 to 249 Ma (Table 4). Examples include the rhyolites of Lücun and Renzhixueshan, which have zircon ages of 247 ± 1.8 Ma (Liu et al. 2011) and 247.4 ± 2.1 Ma to 249 ± 1.6 Ma (Wang et al. 2011), respectively, consistent with the zircon ages of granitoids exposed along the Ailaoshan Belt of 237–247 Ma (Wu et al. 2017). The youngest episode of magmatism in the Jinshajiang–Ailaoshan Belt is related to post-collisional extension. Zircon U–Pb ages of post-collision granitoids such as Jianren and Ludian vary from 214 to 234 Ma (Jian et al. 2003; Zhu et al. 2011; Zi et al. 2013). Our concordant zircon age for samples LS-1 and LS-3 of 250.8 ± 0.6 Ma overlaps the period of pre-collision subduction-related magmatism (Fig. 9). We therefore suggest that zircons in the meta-sandstones associated with the Jinchang Au–Ni deposits were transported from nearby pre-collision magmatic rocks in the Ailaoshan Belt.

Previous studies indicate that the Palaeo-Tethys Ocean opened by seafloor spreading during Early Carboniferous time, leading to the formation of the Jinshajiang ophiolitic mélange (Jian et al. 2009b; Zi et al. 2012b). However, the ophiolite in the Ailaoshan Belt and its northwestern extension in the Jinshajiang did not form simultaneously. Wang et al. (2000) obtained a U–Pb age of 362 ± 41 Ma for plagiogranite in the Ailaoshan Belt. Zircon ages for diabase and plagiogranite from the Ailaoshan ophiolite are 374–387 Ma (Jian et al. 2009b), significantly older than the cumulate gabbro of 343.5 ± 2.7 Ma in the Jinshajiang ophiolite located c. 300 km NW of the Ailaoshan ophiolite (Jian et al. 2009b). Similarly, SHRIMP U–Pb analysis of zircons from the Dongzhulin trondhjemite within the Jinshajiang ophiolite yields a mean $^{206}Pb/^{238}U$ age of 347 ± 7 Ma (Zi et al. 2012b). The c. 347 Ma detrital zircons in chert from the Jinchang mining district match the age of the Jinshajiang ophiolite, but deviate slightly from the Ailaoshan ophiolite age, which is geographically closer to

Jinchang district. The detrital zircons in the auriferous chert may therefore have been derived from the Jinshajiang ophiolite. The morphology of the detrital zircons is sub-rounded to rounded (Fig. 6), consistent with extensive ablation during long-distance transportation from their source regions.

Detrital zircon U–Pb geochronology is commonly applied to provenance analysis by comparing the age distribution pattern with the magmatic history of possible source regions (e.g. Thomas, 2011; Gehrels, 2014; Craddock et al. 2017). Based on a comprehensive comparison of detrital zircon ages from a northern segment of the Ailaoshan Belt with ages from the Indochina Block and western part of South China Block, Wang et al. (2014) suggested that the Ailaoshan Belt belongs to the Simao–Indochina Block and was derived from Indian Gondwana. This interpretation differs from previous interpretations of the South China Block origin (Jian et al. 2009b; Zi et al. 2013; Wu et al. 2017). A comprehensive compilation of zircon U–Pb ages indicates that the western part of the South China Block was not characterized by a pervasive magmatic event during early Palaeozoic time, as indicated by lack of detrital zircons of this age in strata derived from the South China Block (Wang et al. 2014; Yang et al. 2018). The abundance of detrital zircons with a concordant age of 347 ± 1.5 Ma in the auriferous chert sample from the Jinchang mining district therefore supports the interpretation that the Ailaoshan Belt was once united with the Simao Block (Fig. 10).

6.c. Tectonic implications

Since the advent of LA-ICP-MS techniques, zircon trace-element geochemistry has been widely applied to questions of sedimentary provenance and tectono-magmatic processes (e.g. Grimes et al. 2007, 2015; Buret et al. 2017; Schmitt et al. 2017; McKay et al. 2018; Xu et al. 2018; Yan et al. 2018). Because heavy REEs more closely match Zr^{4+} in ionic radius than light REEs do (0.985 Å for Yb^{3+} versus 1.16 Å for La^{3+}, respectively, compared with 0.84 Å for Zr^{4+}), igneous zircons typically display HREE-enriched and light REE (LREE) -depleted patterns (Grimes et al. 2007). Substitution of trivalent REEs for Zr requires charge compensating

Table 4. A compilation of age data for the late Permian – Early Triassic magmatic rocks in the Jinshajiang–Ailaoshan Belt. Magmatism stage classification as described by Zi *et al.* (2013)

Sample location	Sample no.	Rock type	Dating method	Age (Ma, 1σ level)	Data source
Pre-collision subduction-related magmatisms					
Baimaxueshan	TA-13	Granite	LA-ICP-MS	245.2 ± 3.4	Reid *et al.* (2007)
	DQ01-1a	Granodiorite	LA-ICP-MS	254.6 ± 1.8	Zhang *et al.* (2011)
	DQ01-1b	Diorite	LA-ICP-MS	253.5 ± 1.6	Zhang *et al.* (2011)
	SJ133	Granodiorite	SHRIMP	249 ± 2	Zi *et al.* (2012*a*)
	SJ142	Granodiorite	SHRIMP	248 ± 2	Zi *et al.* (2012*a*)
	SJ106	Diorite	SHRIMP	251 ± 2	Zi *et al.* (2012*a*)
	SJ143	Diorite	SHRIMP	250 ± 2	Zi *et al.* (2012*a*)
	SJ109	Tonalite	SHRIMP	253 ± 4	Zi *et al.* (2012*a*)
Xin'anzhai	XAZ13-02	Granodiorite–granite	LA-ICP-MS	257.2 ± 2.2	Yang *et al.* (2018)
	XAZ13-03	Granodiorite–granite	LA-ICP-MS	256.8 ± 1.9	Yang *et al.* (2018)
	HH-43A	Monzogranite	LA-ICP-MS	251.9 ± 1.4	Liu *et al.* (2015)
	HH-45A	Monzogranite	LA-ICP-MS	251.2 ± 1.4	Liu *et al.* (2015)
Laowangzhai	M01	Granite	LA-ICP-MS	251.0 ± 1.4	Wang *et al.* (2014)
Syn-collisional volcanisms and magmatisms					
Lücun	LC2007	Rhyolite	SHRIMP	247.3 ± 1.8	Liu *et al.* (2011)
Maoheshan	MH2007	Basalt	SHRIMP	249 ± 1.6	Liu *et al.* (2011)
Pantiange	SJ22	Rhyolite	SHRIMP	247 ± 3	Zi *et al.* (2012*c*)
	SJ33	Rhyolite	SHRIMP	246 ± 3	Zi *et al.* (2012*c*)
Cuiyibi	10SJ28	Basalt	SHRIMP	245 ± 4	Zi *et al.* (2012*c*)
	SJ82	Basalt	SHRIMP	237 ± 3	Zi *et al.* (2012*c*)
	SJ4	Rhyolite	SHRIMP	232 ± 3	Zi *et al.* (2012*c*)
	SJ44	Rhyodacite	SHRIMP	239 ± 3	Zi *et al.* (2012*c*)
Yinjie	ALN13149	Granitoid	LA-ICP-MS	247.1 ± 2.0	Wu *et al.* (2017)
Majie	ALN0916-1	Granitoid	LA-ICP-MS	241.2 ± 1.0	Wu *et al.* (2017)
	ALN13178	Granitoid	LA-ICP-MS	239.5 ± 1.8	Wu *et al.* (2017)
Yuanjiang	AL06132-2	Granitoid	LA-ICP-MS	237.9 ± 2.6	Wu *et al.* (2017)
Renzhixueshan	JJD03-1	Rhyolite	LA-ICP-MS	247.4 ± 2.1	Wang *et al.* (2011)
	JJD03-11	Rhyolite	LA-ICP-MS	249.1 ± 1.6	Wang *et al.* (2011)
Post-collisional extension-related magmatisms					
Jiaren	LiN	Granodiorite	SIMS	233.1 ± 1.4	Zhu *et al.* (2011)
	LuN	Granodiorite	SIMS	231.0 ± 1.6	Zhu *et al.* (2011)
	BW	Granodiorite	SIMS	233.9 ± 1.4	Zhu *et al.* (2011)
Ludian	005-8	Monzogranite	SHRIMP	214 ± 6	Jian *et al.* (2003)
	SJ22	Monzogranite	SHRIMP	228 ± 2	Zi *et al.* (2013)
	SJ16	Granodiorite	SHRIMP	226 ± 3	Zi *et al.* (2013)
	SJ69	Biotite monzogranite	SHRIMP	220 ± 3	Zi *et al.* (2013)
	SJ72	Biotite granodiorite	SHRIMP	231 ± 3	Zi *et al.* (2013)
	SJ16	Granodiorite	SHRIMP	230 ± 2	Zi *et al.* (2013)

cations in the tetrahedral site; P^{5+} is an ideal candidate for such charge compensation. This coupled substitution may apply to zircons of the Jinchang mining district because YPO_4 contents of the zircons correlate positively with total REE contents ($R^2 = 0.93$; Fig. 11). REE concentrations of zircons from continental and oceanic crust overlap, which complicates the distinction of source-rock composition using zircon geochemistry alone (Grimes *et al.* 2007). Nevertheless, the compilation of Grimes *et al.* (2007)
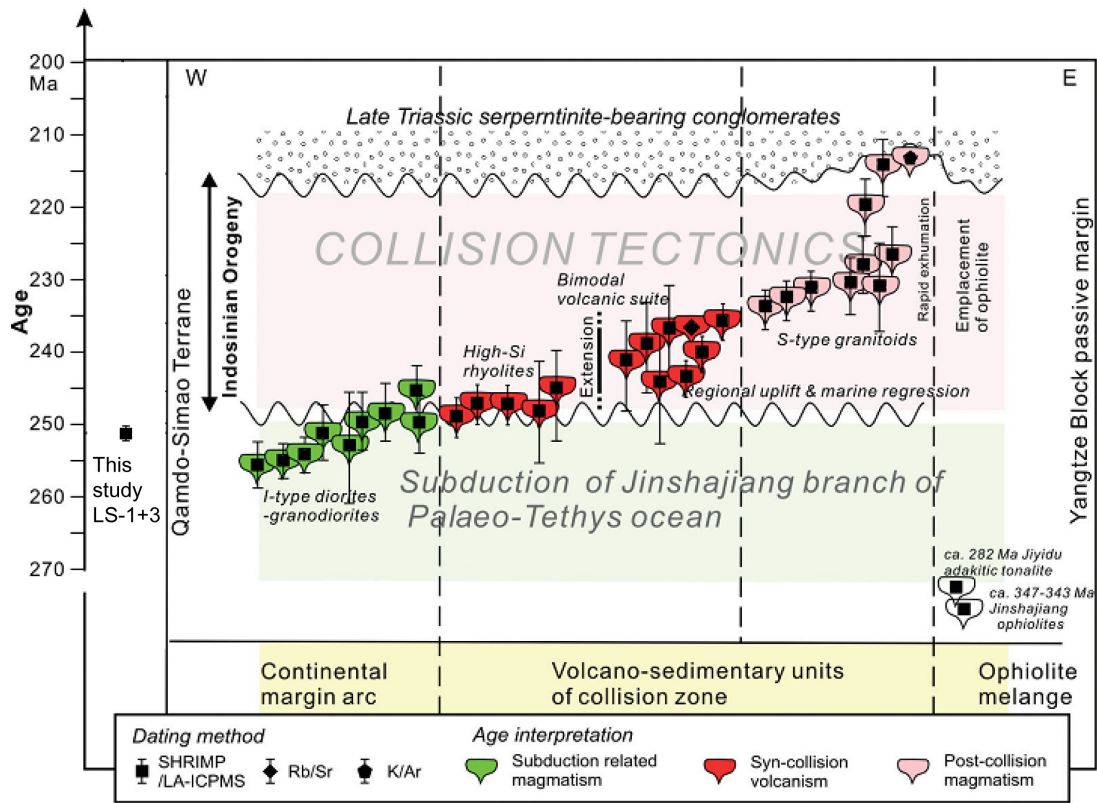
Fig. 9. (Colour online) Concordia age of meta-sandstone sample LS-1+3 compared with temporal distribution of magmatic activities during late Palaeozoic – Triassic time in the Jinshajiang–Ailaoshan Belt and relations with major tectonic events, compiled by Zi *et al.* (2013).
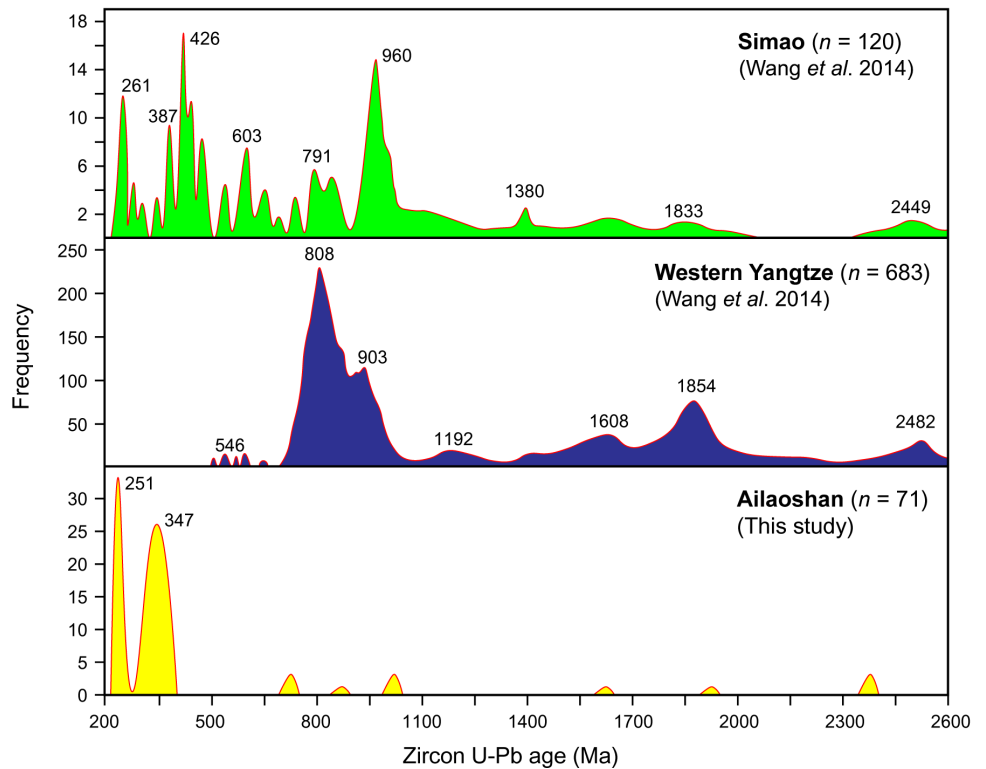
Fig. 10. (Colour online) Comparison of age distribution pattern of detrital zircons from the meta-sandstone and chert with the Simao Block and the South China Block. The curves for the Simao Block and the South China Block are from Wang *et al.* (2014).
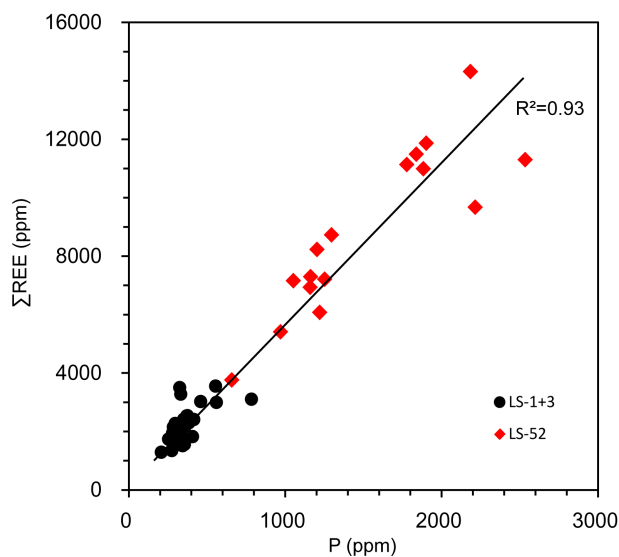
Fig. 11. (Colour online) A positive correlation ($R^2 = 0.93$) between total REE and P concentration in zircons, indicating that P^{5+} and trivalent REEs were incorporated into the Zr site.

indicates that, despite the overlap, zircons from oceanic crust commonly have variable but more elevated REE contents than continental zircons. Zircons from auriferous chert sample LS-52 exhibit REE distribution patterns similar to those of zircons from the meta-sandstone samples, but with higher total REE concentrations (Fig. 8). This indicates that the zircons used for the concordant age calculation of the chert sample may originate from oceanic crust, whereas the zircons from meta-sandstone may derive from a continental source.

Because zircon U, Yb, Y and Hf contents vary among different geologic settings, it is possible to use such data to determine the provenance of continental crust or oceanic crust (e.g. Belousova *et al.* 2002; Grimes *et al.* 2007, 2015; Carley *et al.* 2014). Hf^{4+} and Zr^{4+} are closely similar in ionic radius (0.83 and 0.84 Å, respectively), so Hf is highly compatible in zircon and Hf concentrations can reach weight percent levels. U^{4+} has a larger ionic radius (1.0 Å) than Zr^{4+}, resulting in a lesser compatibility in zircon than Hf. U and Yb have similar compatibility in zircon, but they show different compatibility in magmatic systems; U is enriched in the continental crust relative to the oceanic crust of mid-ocean ridge basalts, whereas Yb is relatively enriched in the oceanic crust (Grimes *et al.* 2007). Yttrium and Hf behave similarly to Yb. As a result of differences in compatibility, these elements and their ratios can distinguish different zircon provenances. Based on a compilation of trace-element compositions of zircons from variable geological settings, Grimes *et al.* (2007, 2015) and Xu *et al.* (2018) suggested that U versus Yb and U/Yb versus Hf, Y and Nb/Yb plots can be used to classify zircons from continental or ocean crust. In our samples, the zircons used for the concordant age calculation from meta-sandstone (LS-1 and LS-3) all fall within the continental crust field (Fig. 12). In combination with the zircon morphology and concordant age, we infer that these zircons were transported from continental-arc magmatic rocks located near the Mojiang site. The widespread exposure of *c.* 250 Ma granitoids along the Ailaoshan Belt also supports intensive magmatism related to the Palaeo-Tethys collision (Reid *et al.* 2007; Liu *et al.* 2011; Zi *et al.* 2012*a*, *c*, 2013; Wang *et al.* 2014; Yang *et al.* 2018). The zircons from chert sample LS-52 fall within the oceanic

crust field (Fig. 12), and are probably from a mid-ocean ridge as suggested by U/Yb versus Nb/Yb plot (Fig. 12d). Mafic rocks of ocean-crust origin of *c.* 347 Ma have been reported along the Jinshanjiang–Ailaoshan Belt; examples include the cumulate gabbro of 343.5 ± 2.7 Ma and the trondhjemite of 347 ± 7 Ma from the Jinshajiang ophiolite (Jian *et al.* 2009*b*; Zi *et al.* 2012*b*). We therefore suggest that the detrital zircons in the chert unit in the Jinchang Au–Ni mining district was likely transported from the Jinshajiang–Ailaoshan ophiolite related to the branch Palaeo-Tethys Ocean seafloor spreading. The zircons in the chert layer derived from the newly formed oceanic crust.

Zircon U–Pb dating suggests that the Ailaoshan ophiolite formed at 387–374 Ma (Jian *et al.* 2009*b*), slightly older than its northwestern extension of the Jinshajiang ophiolite of *c.* 347 Ma (Zi *et al.* 2012*b*). Considering that the chert in the Jinchang mining district in the Ailaoshan Belt and the Jinshajiang ophiolite share similar zircon ages, we suggest that the detrital zircons in the chert were not transported from the nearby Ailaoshan ophiolite, but from the Jinchang ophiolite, which is *c.* 300 km NW of the Ailaoshan ophiolite. The long-distance transportation is further supported by the sub-rounded to rounded shape of zircons in the chert unit. The SE-directed transportation of sedimentary materials indicates that collision after the closure of the Ailaoshan Ocean would be more intensive in the NW segment than in the SE segment. Strong collision and subsequent weathering and erosion created abundant zircons, which were transported SE-wards, probably due to altitude difference. The chert sample has no zircons from the nearby Ailaoshan ophiolite, which may indicate that the Ailaoshan Ocean was still not completely closed during the deposition of chert formation, in line with the theory that the closure of the Ailaoshan Ocean occurred from the NW to the SE. During Palaeozoic – Early Triassic time, subduction-related magmatism was most likely intensive in the entire Ailaoshan Belt because of widespread magmatic rocks with similar ages at both NW and SE segments (Zi *et al.* 2012*a*, 2013). Sedimentary materials of meta-sandstone were dominantly transported from the nearby magmatic rocks as indicated by similar zircon U–Pb ages and their euhedral shapes. The continental crust of the Simao Block served as the source of detrital zircons and other sedimentary materials, which were eroded, transported and finally deposited in nearby basins. The Ailaoshan Belt underwent collision after the closure of the Palaeo-Tethys Ocean.

7. Conclusions

The Ailaoshan Belt in southwestern China is a significant tectono-magmatic-metallogenic province. Our LA-ICP-MS U–Pb geochronological and trace-element study of zircons from the Jinchang Au–Ni deposit in the Ailaoshan Belt yields the following conclusions.

(1) The Yiwanshui Formation meta-sandstone, unconformably overlying the Jinchangyan Formation auriferous chert and slate layers, contain abundant detrital zircons. A group of young zircons yielded a concordant U–Pb age of 250.8 ± 0.6 Ma, constraining the maximum depositional age of the meta-sandstone to the Permian–Triassic boundary.

(2) Detrital zircons from the Jinchangyan Formation chert exhibit variable U–Pb ages; a group of young zircons yielded a concordant U–Pb age of 347.0 ± 1.5 Ma, indicating that the chert formed later than Early Carboniferous time, and not during Silurian or Devonian time as suggested by previous workers.
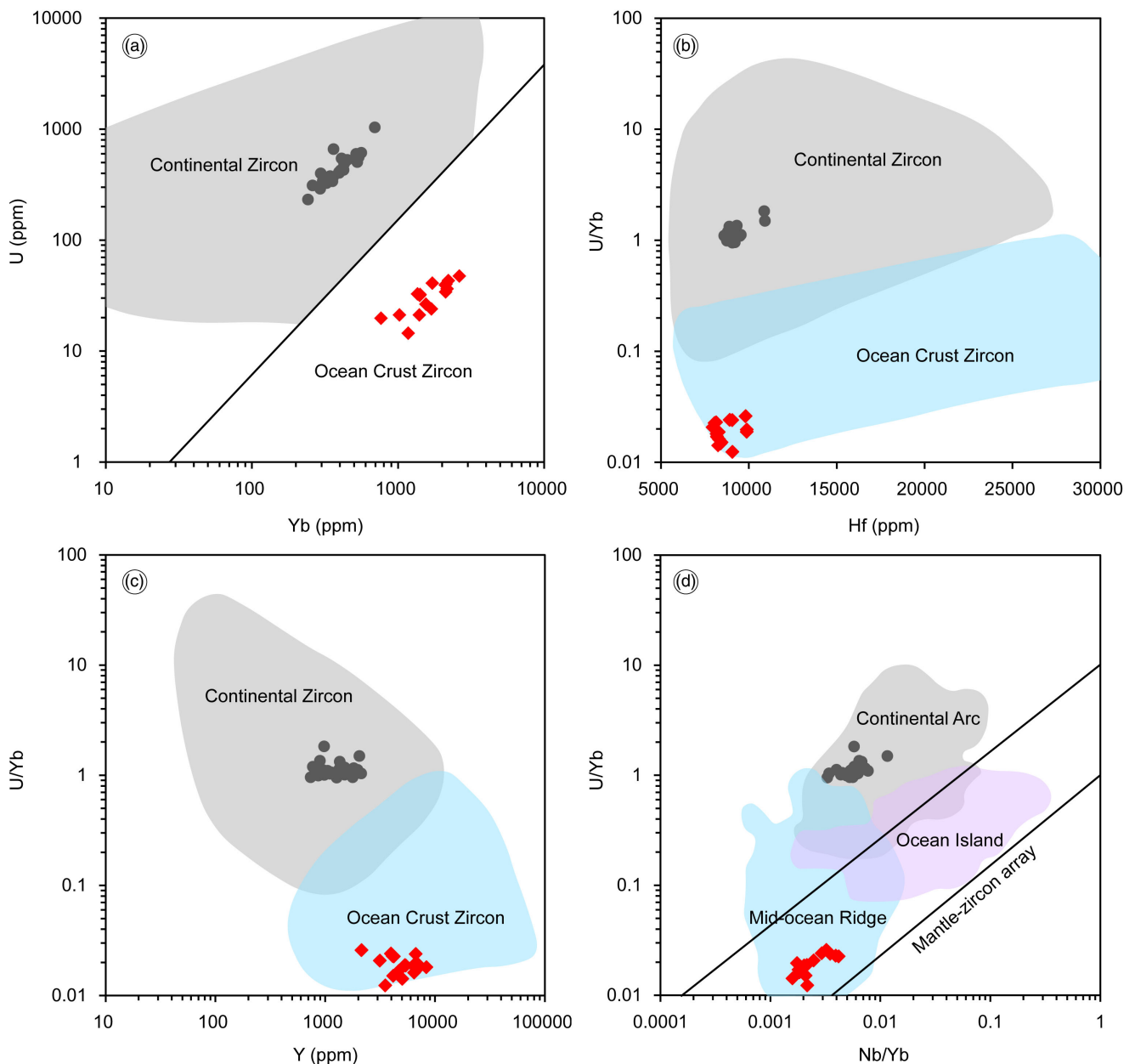
Fig. 12. (Colour online) Application of (a) U v. Yb, (b) U/Yb v. Hf, (c) U/Yb v. Y and (d) U/Yb v. Nb/Yb plots as geochemical discriminant proxies for zircons from variable provenances. The areas of continental zircon and ocean crust zircon are after Grimes *et al.* (2007, 2015).

(3) Zircons in the Yiwanshui Formation meta-sandstone were derived from nearby magmatic rocks of continental crust origin, which were generated by pre-collision subduction-related magmatism related to closure of the Palaeo-Tethys Ocean. Zircons in the Jinchangyan Formation chert were transported long distances from the Jinshajiang ophiolite that were related to seafloor spreading in a branch of the Palaeo-Tethys Ocean.

References

Allegre CJ, Courtillot V, Tapponnier P, Hirn A, Mattauer M, Coulon C, Jaeger JJ, Achache J, Scharer U, Marcoux J, Burg JP, Girardeau J, Armijo R, Gariepy C, Gopel C, Li T, Xiao X, Chang C, Li G, Lin B, Teng J, Wang N, Chen G, Han T, Wang X, Deng W, Sheng H, Cao Y, Zhou J, Qiu H, Bao P, Wang S, Wang B, Zhou Y and Xu R (1984) Structure and evolution of the Himalaya-Tibet orogenic belt. *Nature* **307**, 17–22.

Allen CM, Williams IS, Stephens CJ and Fielding CR (1998) Granite genesis and basin formation in an extensional setting: the magmatic history of the Northernmost New England Orogen. *Australian Journal of Earth Sciences* **45**, 875–88.

Andersen T (2002) Correction of common lead in U-Pb analyses that do not report ^{204}Pb. *Chemical Geology* **192**, 59–79.

Belousova EA, Griffin WL, O'Reilly SY and Fisher NI (2002) Igneous zircons: trace element composition as an indicator of source rock type. *Contributions to Mineralogy and Petrology* **143**, 602–22.

Buret Y, Wotzlaw J-F, Roozen S, Guillong M, von Quadt A and Heinrich CA (2017) Zircon petrochronological evidence for a plutonic-volcanic connection in porphyry copper deposits. *Geology* **45**, 623–26.

Carley TL, Miller CF, Wooden JL, Padilla AJ, Schmitt AK, Economos RC, Bindeman IN and Jordan BT (2014) Iceland is not a magmatic analog for the Hadean: evidence from the zircon record. *Earth and Planetary Science Letters* **405**, 85–97.

Chung S-L, Lee T-Y, Lo C-H, Wang P-L, Chen CY, Yem NT, Hoa TT and Wu G (1997) Intraplate extension prior to continental extrusion along the Ailao Shan-Red River shear zone. *Geology* **25**, 311–14.

Craddock JP, Fitzgerald P, Konstantinou A, Nereson A and Thomas RJ (2017) Detrital zircon provenance of upper Cambrian-Permian strata and tectonic evolution of the Ellsworth Mountains, West Antarctica. *Gondwana Research* **45**, 191–207.

Deng J, Wang Q, Li G and Santosh M (2014) Cenozoic tectono-magmatic and metallogenic processes in the Sanjiang region, Southwestern China. Earth. *Science Review* **138**, 268–99.

Dickinson WR and Gehrels GE (2009) Use of U-Pb ages of detrital zircons to infer maximum depositional ages of strata: a test against a Colorado Plateau Mesozoic database. *Earth and Planetary Science Letters* **288**, 115–25.

Fan W, Wang Y, Zhang A, Zhang F and Zhang Y (2010) Permian arc-back-arc basin development along the Ailaoshan tectonic zone: geochemical, isotopic and geochronological evidence from the Mojiang volcanic rocks, Southwest China. *Lithos* **119**, 553–68.

Fang W, Hu R, Xie G, Su W and Qi L (2001) Diagenetic-metallogenic ages of pyritic cherts and their implications in Mojiang Ni-Au deposits in Yunan Province, China. *Chinese Science Bulletin* **46**, 857–60 (in Chinese).

Gehrels G (2014) Detrital zircon U-Pb geochronology applied to tectonics. *Annual Reviews of Earth and Planetary Science* **42**, 127–49.

Geological Map of Mojiang sheet (1976) Geological map of Mojiang sheet of People's Republic of China, No. F-47-VI, Scale 1:200 000. Second Geological Survey Team of the Yunnan Geological Bureau.

Grimes CB, John BE, Kelemen PB, Mazdab FK, Wooden JL, Cheadle MJ, Hanghøj K and Schwartz JJ (2007) Trace element chemistry of zircons from oceanic crust: a method for distinguishing detrital zircon provenance. *Geology* **35**, 643–46.

Grimes CB, Wooden JL, Cheadle MJ and John BE (2015) "Fingerprinting" tectono-magmatic provenance using trace elements in igneous zircon. *Contributions to Mineralogy and Petrology* **170**, 46.

Hoskin PWO and Schaltegger U (2003) The composition of zircon and igneous and metamorphic petrogenesis. *Reviews in Mineralogy and Geochemistry* **53**, 27–62.

Internal Exploration Report (1982) Exploration report of the Jinchang gold deposit in Mojiang County, Yunnan Province. The Chinese People's Liberation Army of 00533 Force (in Chinese).

Jian P, Liu D, Kröner A, Zhang Q, Wang Y, Sun X and Zhang W (2009a) Devonian to Permian plate tectonic cycle of the Paleo-Tethys Orogen in Southwest China (I): geochemistry of ophiolites, arc/back-arc assemblages and within-plate igneous rocks. *Lithos* **113**, 748–66.

Jian P, Liu D, Kröner A, Zhang Q, Wang Y, Sun X and Zhang W (2009b) Devonian to Permian plate tectonic cycle of the Paleo-Tethys Orogen in southwest China (II): insights from zircon ages of ophiolites, arc/back-arc assemblages and within-plate igneous rocks and generation of the Emeishan CFB province. *Lithos* **113**, 767–84.

Jian P, Liu D and Sun X (2003) SHRIMP dating of Baimaxueshan and Ludian granitoid batholiths, northwestern Yunan Province, and its geological implications. *Acta Geoscientia Sinica* **24**, 337–42 (in Chinese with English abstract).

Lai C-K, Meffre S, Crawford AJ, Zaw K, Halpin JA, Xue C-D and Salam A (2014a) The Central Ailaoshan ophiolite and modern amalogs. *Gondwana Research* **26**, 75–88.

Lai C-K, Meffre S, Crawford AJ, Zaw K, Xue C-D and Halpin JA (2014b) The western Ailaoshan volcanic belts and their SE Asia connection: a new tectonic model for the eastern Indochina block. *Gondwana Research* **26**, 52–74.

Leloup PH, Lacassin R, Tapponnier P, Schärer U, Zhong D, Liu X, Zhang L, Ji S and Trinh PT (1995) The Ailao Shan-Red River shear zone (Yunnan, China), Tertiary transform boundary of Indochina. *Tectonophysics* **251**, 13–84.

Liu C, Deng J, Liu J and Shi Y (2011) Charactristics of volcanic rocks from Late Permian to Early Traissic in Ailaoshan tectono-magmatic belt and implications for tectonic settings. *Acta Petrologica Sinica* **27**, 3590–602.

Liu H, Wang Y, Cawood PA, Fan W, Cai Y and Xing X (2015) Record of Tethyan ocean closure and Indosinian collision along the Ailaoshan suture zone (SW China). *Gondwana Research* **27**, 1292–306.

Liu JL, Wang AJ, Cao SY, Zou YX, Tang Y and Chen Y (2008) Geochronology and tectonic implication of migmatites from Diancangshan, Western Yunnan, China. *Acta Petrologica Sinica* **24**, 413–20 (in Chinese with English abstract).

Liu Y, Hu Z, Zhong K, Gao C, Gao S, Xu J and Chen H (2010) Reappraisement and refinement of zircon U-Pb isotope and trace element analyses by LA-ICP-MS. *Chinese Science Bulletin* **55**, 1535–46.

Ludwig KR (2010) *Isoplot/Ex Version 4.1, A Geochronological Toolkit for Microsoft Excel*. Berkeley Geochronology Center Special Publication: Berkeley, CA, USA, No. 4.

McDonough WF and Sun S-S (1995) The composition of the Earth. *Chemical Geology* **120**, 223–53.

McKay MP, Jr, Jackson WT and Hessler AM (2018) Tectonic stress regime recorded by zircon Th/U. *Gondwana Research* **57**, 1–9.

Metcalfe I (2006) Palaeozoic and Mesozoic tectonic evolution and palaeogeography of East Asian crustal fragments: the Korean Peninsula in context. *Gondwana Research* **9**, 24–46.

Mo X-X, Lu F-X and Shen S-Y (1993) *Sanjiang Tethyan Volcanism and Related Mineralization*. Beijing: Geological Publishing House, 267 pp. (In Chinese).

Pan G, Xu Q, Hou Z, Wang L, Du D, Mo X, Li D, Wang M, Li X, Jiang X and Hu Y (2003) *Archipelagic Orogenesis, Metallogenic Systems and Assessment of the Mineral Resources along the Nüjiang-Lancangjiang-Jinshajiang Area in Southwestern China*. Beijing: Geological Publishing House (in Chinese with English abstract).

Reid A, Wilson CJL, Shu L, Pearson N and Belousova E (2007) Mesozoic plutions of the Yidun Arc, SW China: U/Pb geochronlogy and Hf isotopic signature. *Ore Geology Reviews* **31**, 88–106.

Rubatto D and Gebauer D (2000) Use of cathodoluminescence for U-Pb zircon dating by ion microprobe: some examples from the Western Alps. In *Cathodoluninescence in Geosciences* (eds M Pagel, V Barbin, P Blanc and D Ohnenstetter), pp. 373–400. Berlin: Springer.

Schmitt AK, Klitzke M, Gerdes A and Schäfer C (2017) Zircon hafnium-oxygen isotope and trace element petrochronology of intraplate volcanic rocks from the Eifel (Germany) and implications for mantle versus crustal origins of zircon megacrysts. *Journal of Petrology* **58**, 1841–70.

Sengör AMC (1987) Tectonic of the Tethysides: orogenic collage development in a collisional setting. *Annual Review of Earth and Planetary Sciences* **15**, 213–44.

Sone M and Metcalfe I (2008) Parallel Tethyan sutures in mainland Southeast Asia: new insights for Palaeo-Tethys closure and implications for the Indosinian orogeny. *Comptes Rendus Geoscience* **340**, 166–79.

Steiger RH and Jäger E (1977) Subcommission on geochronology: convention on the use of decay constants in geo- and cosmochronology. *Earth and Planetary Science Letters* **36**, 359–62.

Stewart JH, Gehrels GE, Barth AP, Link PK, Christie-Blick N and Wrucke CT (2001) Detrital zircon provenance of Mesoproterozoic to Cambrian arenites in the western United States and northwestern Mexico. *Geological Society of America Bulletin* **113**, 1343–56.

Surpless KD, Graham SA, Covault JA and Wooden JL (2006) Does the Great Valley Group contain Jurassic strata? Reevaluation of the age and early evolution of a classic foreland basin. *Geology* **34**, 21–24.

Thomas WA (2011) Detrital-zircon geochronology and sedimentary provenance. *Lithosphere* **3**, 304–8.

Wang B-D, Wang L-Q, Wang D-B and Zhang W-P (2011) Zircons U-Pb dating of volcanic rocks from Renzhixueshan Formation in Shangdie rift basin of Sanjiang area and its geological implications. *Acta Petologica et Mineralogica* **30**, 25–33 (in Chinese with English abstract).

Wang Q, Deng J, Li S, Li G, Yu L and Qiao L (2014) The boundary between the Simao and Yangtze blocks and their locations in Gondwana and Rodinia: constraints from detrital and inherited zircons. *Gondwana Research* **26**, 438–48.

Wang Q, Groves DI, Deng J, Li H, Yang L and Dong C (2019) Evolution of the Miocene Ailaoshan orogenic gold deposits, southeastern Tibet, during a complex tectonic history of lithosphere-crust interaction. *Mineralium Deposita* **55**, 1085–104.

Wang X, Metcalfe I, Jian P, He L and Wang C (2000) The Jinshajiang-Ailaoshan Suture Zone, China: tectonostratigraphy age and evolution. *Journal of Asian Earth Sciences* **18**, 675–90.

Wu W, Liu J, Chen X and Zhang L (2017) Zircon U-Pb ages, Hf isotope data, and tectonic implications of Early-Middle Triassic granitoids in the Ailaoshan high-grade metamorphic belt of southeast Tibet. *International Journal of Earth Sciences* **106**, 875–97.

Xie G, Hu R, Fang W and Qi L (2001) Geochemistry of depositional environment of siliceous rocks from Mojiang gold deposit in Yunnan province. *Geochimica* **30**, 491–97 (in Chinese with English abstract).

Xie L, Zhang Y, Zhang H, Sun J and Wu F (2008) In situ simultaneous determination of trace elements, U-Pb and Lu-Hf isotopes in zircon and baddeleyite. *Chinese Science Bulletin* **53**, 1563–73.

Xiong Y (2014) The ore-forming processes of Jinchang hydrothermal gold and nickel deposit, Mojiang, western Yunnan, China. M.Sc. thesis, China University of Geosciences (Beijing), 95 pp. (in Chinese with English abstract). Published thesis.

Xu J, Xia X-P, Cai K, Lai C-K, Liu X-J, Yang Q, Zhou M-L, Ma P-F and Zhang L (2020a) Remnants of a Middle Triassic island are on western margin of South China Block: evidence for bipolar subduction of the Paleotethyan Ailaoshan Ocean. *Lithos* 360–61, https://doi.org/10.1016/j.lithos.2020.105447.

Xu L-G, Kong Z-G, Qu J-F, Li B-L, Qiu Z-Y, Olin P and Danyushevsky L (2020b) Metallogenic model of the Jinchang Au-Ni deposit in the Ailaoshan belt, SW China, determined on the basis of pyrite trace element contents, in-situ sulfur isotope composition and PGE geochemistry.

Ore Geology Reviews **120**, 103415, https://doi.org/10.1016/j.oregeorev.2020.103415.

Xu X, Li Q, Gui L and Zhang X (2018) Detrital zircon U-Pb geochronology and geochemistry of early Neoproterozoic sedimentary rocks from the Northwestern Zhejiang Basin, South China. *Marine and Petroleum Geology* **98**, 607–21.

Yan L-L, He Z-Y, Beier C and Klemd R (2018) Zircon trace element constrains on the link between volcanism and plutonism in SE China. *Lithos* **320–21**, 28–34.

Yang L, Wang Q, Wang Y and Li G (2018) Proto- to Paleo-Tethyan evolution of the eastern margin of Simao block. *Gondwana Research* **62**, 61–74.

Yunnan Bureau of Geology and Mineral Resources (1982) *Regional Geology of Yunan Province*. Geology Publishing House, Beijing, 611 pp. (in Chinese with English Abstract).

Zhang W, Wang L, Wang B, Wang D, Dai J and Liu W (2011) Chronology, geochemistry and petrogenesis of Deqin granodiorite body in the middle section of Jiangde-Weixi arc. *Acta Petrologica Sinica* **27**, 2577–90 (in Chinese with English abstract).

Zhong D (2000) *Paleotethysides in West Yunnan and Sichuan, China*. Beijing: Science Press.

Zhu J-J, Hu R-Z, Bi X-W, Zhong H and Chen H (2011) Zircon U-Pb ages, Hf-O isotopes and whole-rock Sr-Nd-Pb isotopic geochemistry of granitoids in the Jinshajiang suture zone, SW China: constraints on petrogenesis and tectonic evolution of the Paleo-Tethys Ocean. *Lithos* **126**, 248–64.

Zi J-W, Cawood PA, Fan W-M, Tohver E, Wang Y-J and McCuaig TC (2012a) Generation of Early Indosinian enriched mantle-derived granitoid pluton in the Sanjiang Orogen (SW China) in response to closure of the Paleo-Tethys. *Lithos* **140–41**, 166–82.

Zi J-W, Cawood PA, Fan W-M, Tohver E, Wang Y-J, McCuaig TC and Peng T-P (2013) Late Permian-Triassic magmatic evolution in the Jinshangjiang orogenic belt, SW China and implications for orogenic processes following closure of the Paleo-Tethys. *American Journal of Science* **313**, 81–112.

Zi J-W, Cawood PA, Fan W-M, Wang Y-J and Tohver E (2012b) Contrasting rift and subduction related plagiogranites in the Jinshajiang ophiolite, SW China and implications for the paleo-Tethys. *Tectonics* **31**, TC2012, doi: 10.1029/2011TC002937.

Zi J-W, Cawood PA, Fan W-M, Wang Y-J, Tohver E, McCuaig TC and Peng TP (2012c) Triassic collision in the Paleo-Tethys Ocean constrained by volcanic activity in SW China. *Lithos* **144–45**, 145–60.